

This is an Open Access document downloaded from ORCA, Cardiff University's institutional repository: <https://orca.cardiff.ac.uk/id/eprint/124100/>

This is the author's version of a work that was submitted to / accepted for publication.

Citation for final published version:

Hendry, Katharine R., Huvenne, Veerle A.I., Robinson, Laura F., Annett, Amber, Badger, Marcus, Jacobel, Allison W., Ng, Hong Chin, Opher, Jacob, Pickering, Rebecca A., Taylor, Michelle L., Bates, Stephanie L., Cooper, Adam, Cushman, Grace G., Goodwin, Claire, Hoy, Shannon, Rowland, George, Samperiz Vizcaino, Ana, Williams, James A., Achterberg, Eric P., Arrowsmith, Carol, Alexander Brearley, J., Henley, Sian F., Krause, Jeffrey W., Leng, Melanie J., Li, Tao, McManus, Jerry F., Meredith, Michael P., Perkins, Rupert and Woodward, E. Malcolm S. 2019. The biogeochemical impact of glacial meltwater from Southwest Greenland. *Progress in Oceanography* 176, 102126. 10.1016/j.pocean.2019.102126

Publishers page: <http://dx.doi.org/10.1016/j.pocean.2019.102126>

Please note:

Changes made as a result of publishing processes such as copy-editing, formatting and page numbers may not be reflected in this version. For the definitive version of this publication, please refer to the published source. You are advised to consult the publisher's version if you wish to cite this paper.

This version is being made available in accordance with publisher policies. See <http://orca.cf.ac.uk/policies.html> for usage policies. Copyright and moral rights for publications made available in ORCA are retained by the copyright holders.



1 **The biogeochemical impact of glacial meltwater from Southwest Greenland**

2

3 Katharine R. Hendry¹, Veerle A. I. Huvenne², Laura F. Robinson¹, Amber Annett³, Marcus
4 Badger⁴, Allison W. Jacobel^{5,6}, Hong Chin Ng¹, Jacob Opher⁷⁻⁹, Rebecca A. Pickering^{10,11},
5 Michelle L. Taylor¹², Stephanie L. Bates¹, Adam Cooper³, Grace G. Cushman⁵, Claire
6 Goodwin¹³, Shannon Hoy¹⁴, George Rowland¹, Ana Samperiz^{1,15}, James A. Williams¹⁵, Eric P.
7 Achterberg¹⁶, Carol Arrowsmith¹⁷, J. Alexander Brearley⁷, Sian F. Henley¹⁸, Jeffrey W.
8 Krause^{10,11}, Melanie J. Leng^{17,19}, Tao Li¹, Jerry F. McManus⁵, Michael P. Meredith⁷, Rupert
9 Perkins¹⁵, and E. Malcolm S. Woodward²⁰

10

11 ¹ School of Earth Sciences, University of Bristol, Wills Memorial Building, Queen's Road,
12 Bristol, BS8 1RJ, UK

13 ² National Oceanography Centre, University of Southampton Waterfront Campus, European
14 Way, Southampton, SO14 3ZH, UK

15 ³ Ocean and Earth Science, University of Southampton, Waterfront Campus, European Way,
16 Southampton, SO14 3ZH, UK

17 ⁴ School of Environment, Earth & Ecosystem Sciences, The Open University, Walton Hall,
18 Milton Keynes, MK7 6AA, UK

19 ⁵ Lamont-Doherty Earth Observatory, Columbia University, 61 US-9W, Palisades, NY 10964,
20 USA

21 ⁶ Environment and Society, Brown University, 85 Waterman Street, Providence, RI 02912,
22 USA

23 ⁷ British Antarctic Survey, High Cross, Madingley Road, Cambridge, CB3 0ET, UK

24 ⁸ Centre for Ocean and Atmospheric Sciences, School of Environmental Sciences, University
25 of East Anglia, Norwich Research Park, Norwich NR4 7TJ, UK

26 ⁹ Centre for Environment Fisheries and Aquaculture Science, Pakefield Road, Lowestoft,
27 Suffolk NR33 0HT, UK

28 ¹⁰ Dauphin Island Sea Laboratory, 101 Bienville Boulevard, Dauphin Island, AL 36528, USA

29 ¹¹ University of South Alabama, Mobile, AL, 36688, USA

30 ¹² School of Biological Sciences, University of Essex, Wivenhoe Park, Colchester, CO4 3SQ, UK

31 ¹³ Huntsman Marine Science Centre, 1 Lower Campus Rd, Saint Andrews, NB E5B 2L7,
32 Canada

33 ¹⁴ Center for Coastal & Ocean Mapping/Joint Hydrographic Center, Jere A. Chase Ocean
34 Engineering Lab, 24 Colovos Road, Durham, New Hampshire 03824, USA

35 ¹⁵ School of Earth and Ocean Sciences, Cardiff University, Main Building, Park Place, Cardiff,
36 CF10 3AT, UK

37 ¹⁶ GEOMAR Helmholtz Centre for Ocean Research, Kiel, Wischhofstraße 1-3, D-24148 Kiel,
38 Germany

39 ¹⁷ NERC Isotope Geosciences Facility, British Geological Survey, Keyworth, Nottingham,
40 NG12 3GG, UK

41 ¹⁸ School of GeoSciences, University of Edinburgh, James Hutton Road, Edinburgh, EH9 3FE,
42 UK

43 ¹⁹ Centre for Environmental Geochemistry, School of Biosciences, Sutton Bonington Campus,
44 University of Nottingham, Loughborough, LE12 5RD, UK.

45 ²⁰ Plymouth Marine Laboratory, Prospect Place, The Hoe, Plymouth, PL1 3DH, UK

46 *Corresponding author: K.Hendry@bristol.ac.uk

47

48 **Abstract**

49 Biogeochemical cycling in high-latitude regions has a disproportionate impact on
50 global nutrient budgets. Here, we introduce a holistic, multi-disciplinary framework for
51 elucidating the influence of glacial meltwaters, shelf currents, and biological production on
52 biogeochemical cycling in high-latitude continental margins, with a focus on the silica cycle.
53 Our findings highlight the impact of significant glacial discharge on nutrient supply to shelf
54 and slope waters, as well as surface and benthic production in these regions, over a range of
55 timescales from days to thousands of years. Whilst biological uptake in fjords and strong
56 diatom activity in coastal waters maintains low dissolved silicon concentrations in surface
57 waters, we find important but spatially heterogeneous additions of particulates into the
58 system, which are transported rapidly away from the shore. We expect the glacially-derived
59 particles – together with biogenic silica tests – to be cycled rapidly through shallow
60 sediments, resulting in a strong benthic flux of dissolved silicon. Entrainment of this benthic
61 silicon into boundary currents may supply an important source of this key nutrient into the
62 Labrador Sea, and is also likely to recirculate back into the deep fjords inshore. This study
63 illustrates how geochemical and oceanographic analyses can be used together to probe
64 further into modern nutrient cycling in this region, as well as the palaeoclimatological

65 approaches to investigating changes in glacial meltwater discharge through time, especially
66 during periods of rapid climatic change in the Late Quaternary.

67

68 **Keywords**

69 Biogeochemistry, nutrients, glaciers, primary production, silica cycling

70

71 **Highlights**

72 • Novel multi-disciplinary approach to tracing freshwater and particle transport into
73 boundary currents;

74 • Significant glacial inputs reach coastal waters and are transported rapidly offshore;

75 • Low surface water dissolved silicon concentrations maintained by diatom activity
76 despite strong glacial and benthic supplies.

77

78 **1. Introduction**

79 The high-latitude regions are experiencing some of the most rapid environmental
80 changes observed globally in recent decades. This is particularly true for the Arctic. Here,
81 temperatures are rising twice as fast as the global mean, the Nordic Seas are warming at an
82 accelerated rate (Alexeev, Walsh, Ivanov, Semenov & Smirnov, 2017), Arctic sea-ice is
83 thinning and moving faster (Lindsay & Schweiger, 2015), and multi-year Arctic sea-ice is
84 declining (Maslanik, Fowler, Stroeve, Drobot, Zwally et al., 2007), with significant
85 implications for the interaction between the atmosphere and the oceans (Provost,
86 Sennéchaël, Miguet, Itkin, Rösel et al., 2017). The Greenland Ice Sheet (GrIS) is experiencing
87 significant mass loss largely through surface melting but also via ice discharge at glacier
88 fronts (Enderlin, Howat, Jeong, Noh, Van Angelen et al., 2014; Felikson, Bartholomäus,
89 Catania, Korsgaard, Kjær et al., 2017; van den Broeke, Box, Fettweis, Hanna, Noël et al.,
90 2017). This melting is likely to have a global impact: the North Atlantic receives freshwater
91 from the Nordic Seas, GrIS, and the Canadian Arctic (Bamber, Tedstone, King, Howat,
92 Enderlin et al., 2018), which influences the density structure, circulation, and stratification in
93 regions where deep water-masses form; these represent a major component of ocean
94 circulation that drives global fluxes of heat and freshwater (Carmack, Yamamoto-Kawai,
95 Haine, Bacon, Bluhm et al., 2016; Proshutinsky, Dukhovskoy, Timmermans, Krishfield &
96 Bamber, 2015; Yang, Dixon, Myers, Bonin, Chambers et al., 2016). In addition to freshwater
97 budgets, there has been increasing focus on the role of glaciers and ice sheets in supplying
98 organic material and inorganic nutrients to marine systems. There are significant fluxes of
99 nutrients in GrIS runoff both in dissolved and particulate form, including nitrogen (Wadham,
100 Hawkings, Telling, Chandler, Alcock et al., 2016), phosphate (Hawkings, Wadham, Tranter,
101 Telling, Bagshaw et al., 2016), dissolved silicon (Hawkings, Wadham, Benning, Hendry,
102 Tranter et al., 2017; Meire, Meire, Struyf, Krawczyk, Arendt et al., 2016), and iron (Bhatia,
103 Kujawinski, Das, Breier, Henderson et al., 2013; Hawkings, Wadham, Tranter, Raiswell,
104 Benning et al., 2014). The extent to which these nutrients reach the coastal oceans, and are
105 subsequently advected or mixed from the continental shelves into the open oceans via
106 boundary currents, is poorly constrained and a matter of debate (Hopwood, Bacon, Arendt,
107 Connelly & Statham, 2015). Both dissolved nutrient and particulate dynamics are
108 significantly impacted by circulation processes (Hopwood et al., 2015) and biological activity
109 within glacially-influenced fjords. These regions could be a significant trap of dissolved

110 inorganic phases (Meire, Mortensen, Meire, Juul-Pedersen, Sejr et al., 2017), and have the
111 potential to prevent the nutrient-rich glacial waters reaching the coastal seas. Despite this
112 possibility, distal summer phytoplankton blooms have been detected off Southwest
113 Greenland in association with glacial melt (Arrigo, van Dijken, Castelao, Luo, Rennermalm et
114 al., 2017) and ecosystem models indicate sensitivity to meltwater input (Oliver, Luo,
115 Castelao, van Dijken, Mattingly et al., 2018). An understanding of how natural resources –
116 including fisheries, bird, and mammal stocks that are essential for food and encouraging
117 tourism – will respond in the future to increasing anthropogenic stress on a regional and
118 global scale relies on an understanding of foundational processes of these ecosystem
119 services, including marine biogeochemistry and the sources and sinks of essential nutrients
120 (Berthelsen, 2014; Meire et al., 2017; Weatherdon, Magnostan, Rogers, Sumaila & Cheung,
121 2016).

122 The overarching goal of the Isotope Cycling in the Labrador Sea (ICY-LAB;
123 icylab.wordpress.com) study is to understand the cycling of nutrients in the climatically
124 critical but understudied regions of the Labrador Sea and Greenland fjords. The approach of
125 ICY-LAB is to capture the whole biogeochemical system in these areas of marked
126 environmental change using carefully planned field sampling strategies, with research
127 expeditions to coastal Greenland and the open ocean Labrador Sea. The principal dataset
128 was collected during an oceanic expedition on the RRS *Discovery* (DY081, July-August 2017),
129 with the aim to investigate the influence of glacial meltwater on nutrient cycling in the shelf
130 seas off SW Greenland. Particular focus was placed on the silica budget and how this is
131 framed within the oceanographic and biological processes acting on the W Greenland
132 margin. Uniquely, we combined a range of both traditional and novel methodologies to
133 detect and trace meltwater and glacial material from the shelf across the slope, and to
134 investigate the biogeochemical and biological impact of these inputs. Bringing these
135 different approaches together is essential in these margin environments to obtain a full
136 picture of biogeochemical cycling, providing a robust insight into the system over a range of
137 spatial and temporal scales that are otherwise challenging to resolve (Figure 1).

138

139 **2. Methods and materials**

140

141 **2.1. Fieldwork rationale**

142 The data presented in this paper were collected during expedition DY081, centred on
143 the coastal shelf and slope regions off Southwest Greenland. Model results indicate that this
144 region is influenced by surface meltwater from the Western GrIS, in addition to a significant
145 input of freshwater delivered from the Eastern GrIS via the strong East Greenland Current
146 (EGC) (Luo, Castelao, Rennermalm, Tedesco, Bracco et al., 2016). The study locations were
147 selected to represent this conduit to the open ocean for glacial runoff from the Western and
148 Southwestern GrIS, which have been the focus of recent terrestrial studies carried out in
149 collaboration with the Bristol Glaciology Centre (Hawkings, Hatton, Hendry, de Souza,
150 Wadham et al., 2018; Hawkings et al., 2017). Full details of the oceanographic setting are
151 given in Appendix A.

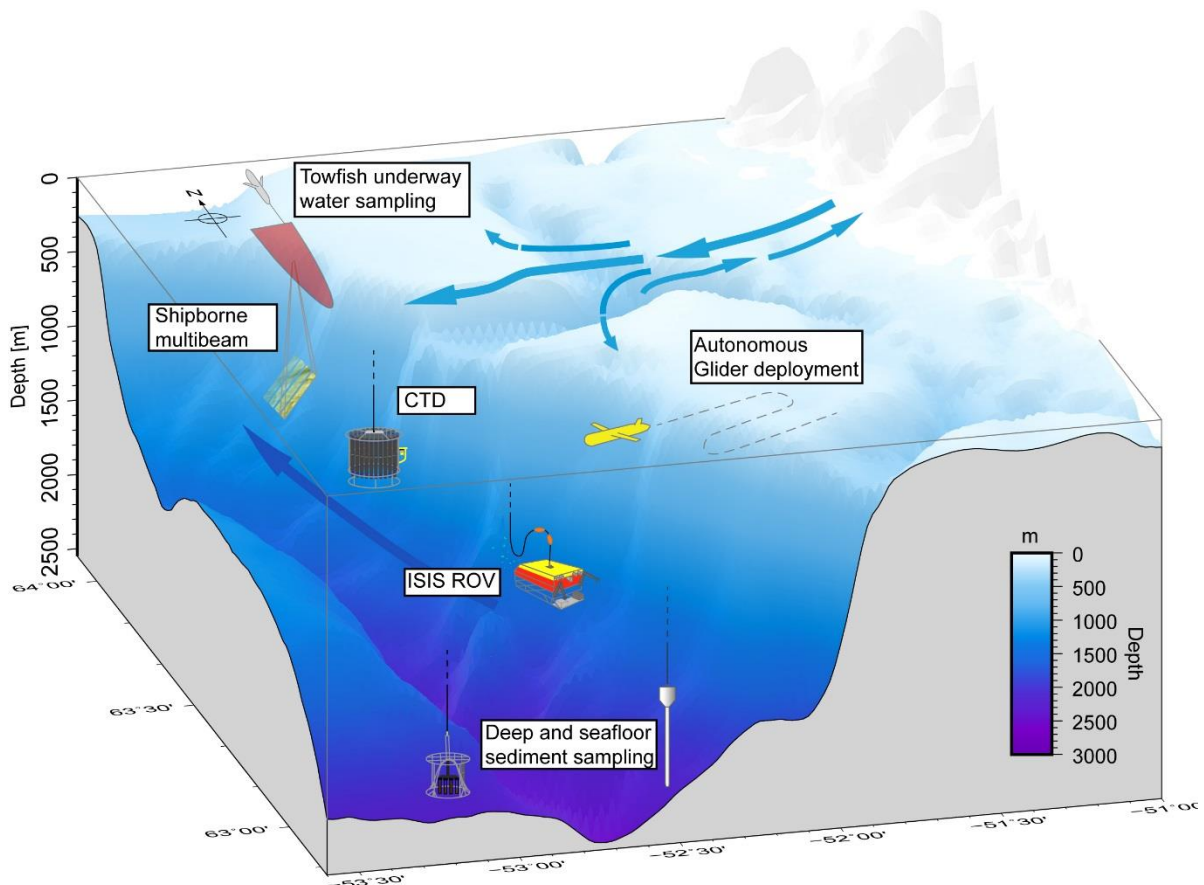


Figure 1: Summary figure showing the multi-discipline approach taken during expedition DY081 of project ICY-LAB.

152

153 We selected the main study location for the ICY-LAB project (“Gothåb (Nuuk) Trough”,
 154 Figure 2a) to be adjacent to Nuuk, which has experienced increasing glacial run-off in recent
 155 years (Van As, Andersen, Petersen, Fettweis, Van Angelen et al., 2014). During DY081,
 156 Southern Greenland was strongly influenced by both icebergs and sea ice, but two sites
 157 (“Narsaq” and “Cape Farewell”, Figure 2a) were still selected there for providing glacial
 158 troughs that could act as direct comparisons to the further north Nuuk site further north.
 159 Orphan Knoll, on the western margin of the Labrador Sea, was selected as a distal
 160 comparison site, and for complementary palaeoclimate, biological and habitat mapping
 161 studies (Figure 2a).

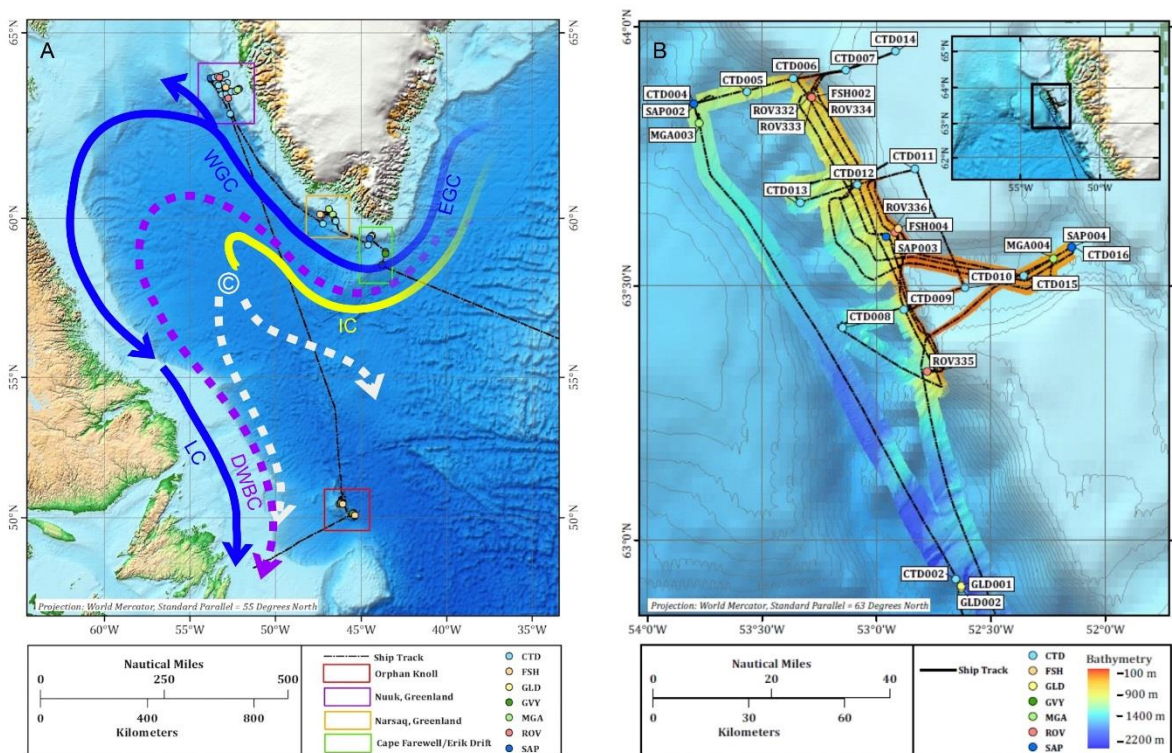


Figure 2: A) Map showing route and main working areas of expedition DY081. Produced in Mercator projection with a standard parallel of 55°N. Arrows show the main current systems in the Labrador Sea: Irminger Current (IC in yellow), West and East Greenland Currents and Labrador Current (WGC, EGC, LC in blue), and the Deep Western Boundary Current (DWBC). Cold, deep polar overflow waters are represented by the purple arrow. The main site of deep-water convection is marked by C, and represented by white arrows. B) Map of Nuuk grid location with ship track, bathymetry and station locations. Produced in Mercator projection with a standard parallel of 63°N.

162
 163 The unique holistic observational approach we took is illustrated in Figure 1, and
 164 included (a) initial bathymetric mapping using acoustic methods (multibeam echosounders)
 165 to increase our understanding of the local terrain and to enable accurate planning of further

166 sampling activities; (b) characterisation of the water column structure using CTD casts and
167 glider deployments; (c) sampling of surface and bottom waters for biogeochemical analyses
168 using the CTD rosette and a trace metal clean towfish; (d) sampling of seabed sediments
169 using a megacorer (for geochemical studies of pore waters) and gravity corer (for
170 palaeoceanographic investigations); (e) seabed observations and precision sampling for
171 biological, palaeoceanographic and sedimentological studies using a work-class scientific
172 ROV.

173

174 **2.2. On-board methodologies and additional laboratory techniques**

175 *2.2.1. Mapping and acoustics*

176 During DY081, multiple acoustic systems were deployed on the ship (e.g. EM122
177 multibeam echosounder (12 kHz); EM710 multibeam echosounder; SBP120 sub-bottom
178 echosounder (2.5 – 6.5 kHz)). These were coordinated via a K-Sync system to avoid
179 interference and crosstalk.

180 Bathymetry data were processed on-board with the Caris HIPS & SIPS software v.8, using
181 standard settings and procedures (data import, navigation and attitude check, application of
182 a “zero tide”, gridding into a 25 mx25 m pixel BASE surface). Backscatter data were
183 processed with Fledermaus FMGT, again using default settings.

184

185 *2.2.2. Physical oceanography*

186 High-resolution water column studies surrounding the prominent glacial Gothåb (Nuuk)
187 Trough were carried out utilising both a grid of Conductivity Temperature Depth (CTD) casts
188 and the deployment of two 1000m-rated Slocum gliders (Figure 2). CTD casts were also used
189 at the south Greenland and Orphan Knoll study sites. Hydrographic analysis enabled
190 characterization of the water column structure in each study location, specifically to locate
191 and quantify the freshwater inputs at the Greenland sites. Salinity was calibrated using
192 bottle samples collected at discrete depths. After laboratory calibration of these samples,
193 no drift corrections were required. Overall errors for temperature were 0.0006 °C (based on
194 laboratory calibration) and 0.002 for salinity. Prior to analysis, data from these stations were
195 gridded to a vertical and horizontal resolution of 10 m and 6 km respectively.

196 Vessel Mounted Acoustic Doppler Current Profilers (VMADP at 75 and 150kHz; Teledyne
197 RD instruments) were secured onto the drop keel in surface waters near the centre-line and

198 beneath the *RRS Discovery*, and used to measure the horizontal current velocity profile.
199 Bottom tracking data were only collected from the 150 kHz instrument intermittently
200 between 18th July and 24th July 2017 while close to Nuuk. In addition, downward and
201 upward looking lowered 300 kHz ADCPs (LADCPs) were mounted on the CTD rosette. LADCP
202 data were processed using LDEO LADCP processing software version IX_8, run on Matlab.
203 Full details of the other sensors attached to the CTD rosette and gliders can be found
204 elsewhere (Hendry, 2017).

205

206 *2.2.3. Biogeochemistry and chemical oceanography*

207 *2.2.3.1. Water column*

208 Water column samples were collected using Niskin bottles attached to the CTD
209 rosette (10L volume) and the Remotely Operated Vehicle (ROV) *Isis* (4 L volume), and via a
210 trace-metal clean towfish. The towfish system comprised of a weighted titanium bodied fish
211 lowered into the water at the stern and streamed as far from the ship as possible. When
212 towed it was at approximately 2m depth, and water was pumped into the ship's labs
213 through an ultra-clean pump and tubing. Trace-metal sampling was only carried out when
214 the ship was moving at speeds greater than 0.5 knots in order to avoid contamination from
215 the hull of the vessel. Four stand-alone pumps (SAPs) were also deployed at key locations to
216 collect water column particles.

217 Samples of seawater were collected for inorganic macronutrients, water oxygen
218 isotope composition ($\delta^{18}\text{O}$) and carbonate chemistry parameters (pH, alkalinity), which are
219 used for investigating freshwater input in high-latitude regions (Hendry, Pyle, Barney Butler,
220 Cooper, Fransson et al., 2018; Meredith, Brandon, Wallace, Clarke, Leng et al., 2008;
221 Thomas, Shadwick, Dehairs, Lansard, Mucci et al., 2011). Phytoplankton pigments were
222 analysed on board, and compared to sensor-derived fluorescence data, to assess algal
223 standing stocks in relation to meltwater input. Full details of sampling methods and
224 laboratory techniques are available in Appendix B.

225

226 *2.2.3.2. Diatom productivity*

227 Biogenic silica (bSiO_2) production (i.e. diatom productivity) analyses were done using
228 radioisotope ^{32}Si as detailed in Krause, Brzezinski and Jones (2011). Briefly, samples were
229 collected within the euphotic zone (sample depths based on light and relative to irradiance

230 just below the surface) and dispensed into acid-cleaned 125 mL polycarbonate bottles. 322
231 Bq of $^{32}\text{Si}(\text{OH})_4$ was added to each sample, and bottles were incubated on deck in surface-
232 seawater-cooled incubators covered with neutral density screening to mimic the depth of
233 collection. After incubation, samples were filtered through 1.2 μm pore size polycarbonate
234 membrane filters. Particulate ^{32}Si activity was quantified using a GM-25 Multicounter (Risø
235 DTU National Laboratory, Denmark) after the samples had aged into secular equilibrium
236 with the short-lived daughter isotope, ^{32}P .

237

238 2.2.3.3. *Radium isotopes*

239 To investigate the fate of solutes sourced from benthic sediments or glacial meltwater,
240 large-volume surface samples for radium (Ra) isotope analysis were collected from the
241 trace-metal clean towfish system, both when the ship was underway ($\sim 2\text{m}$ water depth) and
242 stationary ($\sim 5\text{m}$ water depth). A total of 200-300 L of seawater from a single sampling event
243 were then passed through a plastic column holding MnO_2 -coated acrylic fibre, which
244 quantitatively binds Ra in the sample. The fibers and adsorbed Ra isotopes were then rinsed
245 with deionized water (Milli-Q, Millipore), dried to an appropriate moisture content and
246 loaded into a Ra Delayed Coincidence Counter (RaDeCC; Scientific Computer Instruments,
247 USA) so as to quantify ^{223}Ra and ^{224}Ra content following the methods of Moore and Arnold
248 (1996) and Moore (2008). Each sample was counted 4 times over ~ 4 months to determine
249 the activities of excess ^{224}Ra and ^{223}Ra , above the activities supported by their parent
250 isotopes in the water column (^{228}Th and ^{227}Ac , respectively). Detector efficiencies were
251 determined and monitored regularly at sea and in the laboratory with standards (Annett,
252 Henley, Van Beek, Souhaut, Ganeshram et al., 2013). Final reported activities have been
253 corrected for any decay that occurred between sample collection and analysis, activity
254 supported by parent isotopes, detector background, and efficiency.

255

256 2.2.3.4. *Sediment-water interface*

257 High-latitude ocean margin sediments are increasingly being recognised as an
258 important source of inorganic nutrients and key elements (Henley, Jones, Venables,
259 Meredith, Firing et al., 2018; Kuzyk, Gobeil, Goñi & Macdonald, 2017; Sherrell, Annett,
260 Fitzsimmons, Rocanova & Meredith, 2018). To investigate the role of sediments in these
261 glacially-influenced shelf and slope environments, we collected pore-fluid samples at coastal

262 Greenland and the Labrador Sea. Short sediment cores (≤ 40 cm) were acquired from the
263 study area with a mega corer. Using Rhizon filters (0.15 μm , Rhizosphere Research
264 Products), pore water was extracted from the sediment cores and filtered into syringes, and
265 the samples were stored under cool conditions prior to analysis. Pore water dissolved silicon
266 concentrations were analysed on-board and post-expedition using a V-1200 Vis
267 spectrophotometer, employing a standard molybdate-blue methodology (using Hach Lange
268 reagents). The samples were corrected for blank and calibrated against a ten-point curve
269 that was developed using Si standards of known concentrations. In addition to mega-cores,
270 we also employed ROV push cores to obtain short sediment cores for pore-fluid sampling, in
271 regions where complex bathymetry or the presence of ice-rafted material precluded the use
272 of a megacorer.

273

274 2.2.4. *Palaeoclimate*

275 Two samples types were collected for palaeoclimate research – fossil deep-sea corals
276 and sediment cores. ROV operations were the primary tool for benthic biological and fossil
277 coral collections using grab or suction devices. In addition, where large fossil coral
278 graveyards were observed, a net was used to sample fossil corals. Gravity cores were also
279 collected to obtain long-term records of changes in meltwater flux and iceberg dynamics
280 over the Late Quaternary, thereby providing a longer-term temporal context to the broader
281 data set. Megacores, collected primarily for biogeochemical studies, were also subsampled
282 to provide core-top material that could potentially replace any sections lost from the gravity
283 cores during retrieval.

284

285 2.3. Mass balance calculations

286 To calculate the freshwater mass balance in the study area, the seawater samples are
287 presumed to comprise a mixture of three source water end-members: ocean, sea ice melt
288 and meteoric water, which is assumed to be dominated by glacial discharge. The three end-
289 member assumption enables quantification of the freshwater fractions via the following
290 mass balance equations (Meredith, Heywood, Dennis, Goldson, White et al., 2001):

291

292

293

$$F_{ir} + F_{me} + F_{si} = 1$$
$$F_{ir}S_{ir} + F_{me}S_{me} + F_{si}S_{si} = S_{ms}$$

294

$$F_{ir}\delta_{ir} + F_{me}\delta_{me} + F_{si}\delta_{si} = \delta_{ms}$$

295

296 Where F_{ir} , F_{me} , F_{si} are the calculated fractions of Irminger Water, meteoric and sea ice melt
297 respectively (Irminger Water being the chosen ocean endmember), which sum to 1 by
298 definition. The result is clearly dependent on the exact choice of endmembers for salinity
299 (S_{ir} , S_{me} , S_{si}) and $\delta^{18}\text{O}$ (δ_{ir} , δ_{me} , δ_{si}) for the Irminger Water, meteoric and sea ice melt
300 respectively. S_{ms} and δ_{ms} are the measured salinity and $\delta^{18}\text{O}$ of each sample.

301 Properties for the sea ice melt and meteoric endmembers (Table 1) were based on values
302 reported in Dodd, Heywood, Meredith, Naveira-Garabato, Marca et al. (2009); Melling and
303 Moore (1995); Meredith et al. (2001); and the CTD observations from the DY081 research
304 cruise. Note that negative sea ice melt percentages reflect a net sea ice formation from the
305 water parcel sampled.

306

307 **3. Results**

308

309 EM-122 multibeam swath bathymetry datasets (e.g. Figure 2) are now published on
310 PANGAEA (doi: 10.1594/PANGAEA.892825). The full water column data from CTD profiles
311 and bottles (hydrography, oxygen isotopes, carbonate chemistry, macronutrients e.g. Figure
312 3) are published on PANGAEA (doi.pangaea.de/10.1594/PANGAEA.896544). Here we
313 present a subset of the results, focusing on characterisation of the silica cycle in the water
314 column and sediments.

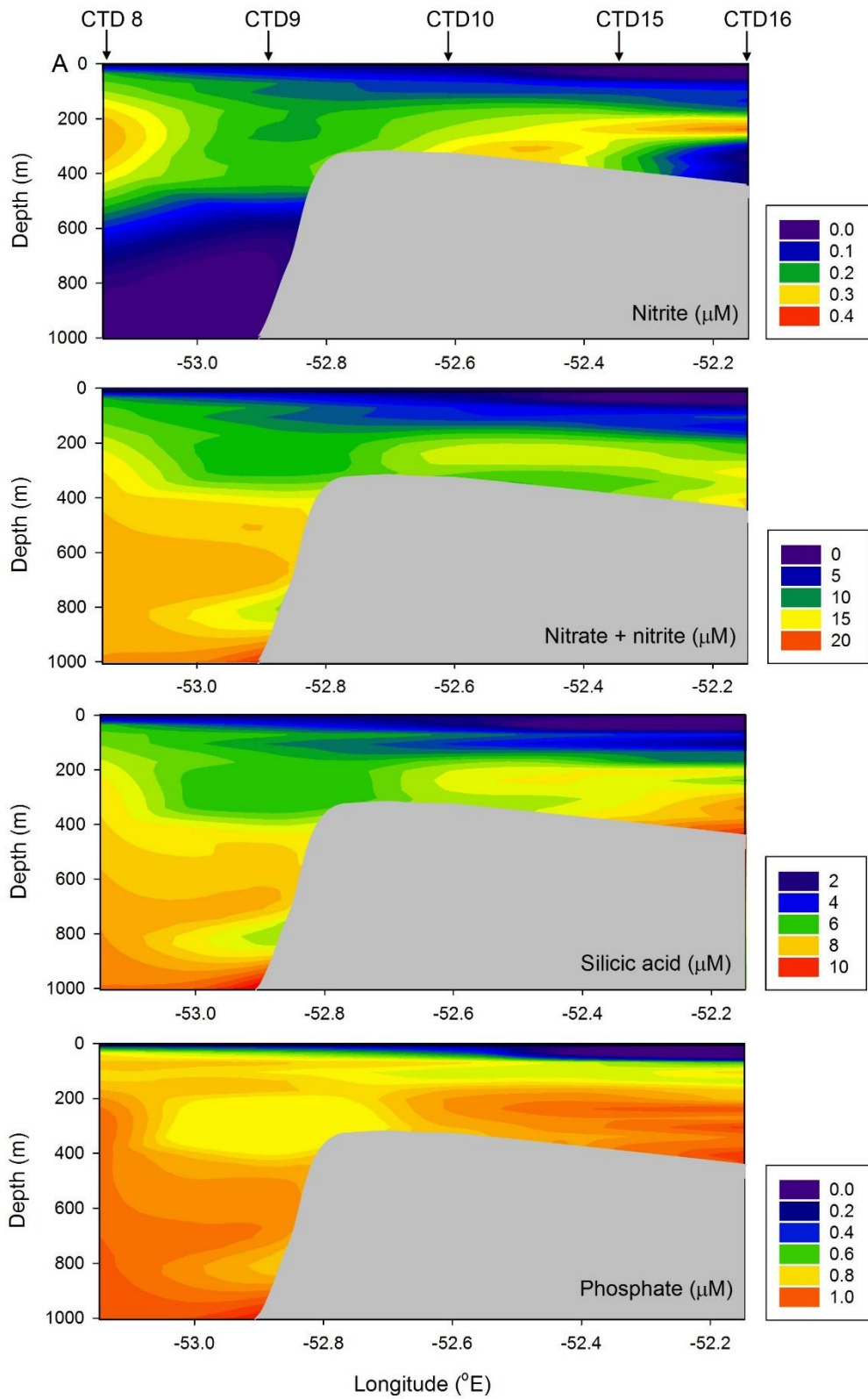
315

316 **3.1. Silica cycling parameters in the water column and sediments**

317

318 *3.1.1. Water column macronutrients and pigments*

319 The nearshore macronutrient concentrations were typically low ($< 11 \mu\text{M}$ nitrate, < 0.2
320 μM nitrite, $< 0.75 \mu\text{M}$ phosphate and $< 5 \mu\text{M}$ DSi in the upper 50 m of the water column)
321 reaching minima in the surface waters with lowest salinity and lowest $\delta^{18}\text{O}$ (an example of
322 which is given in Figure 3a, see also Appendix C). Sections of CTD macronutrient and
323 pigment bottle data from the Nuuk grid, integrated over the top 50m, reveal consistent
324 onshore-offshore trends (an example of which is given in Figure 3b, see also Appendix B).
325 Integrated macronutrient concentrations decreased towards shore concurrent with an



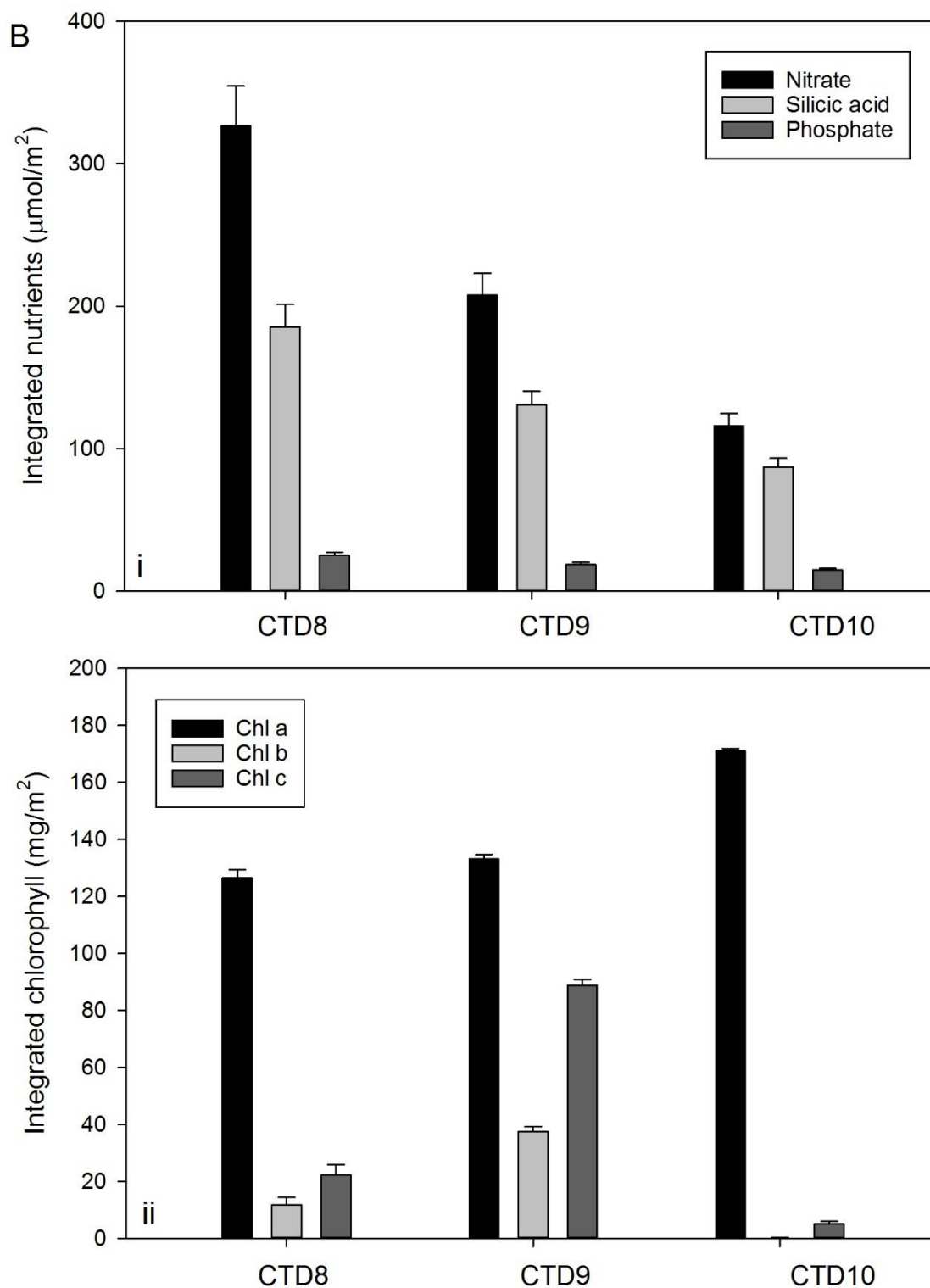


Figure 3: A) Example cross section of macronutrient concentrations from the Nuuk grid (from CTD 8 to CTD 16), showing (from top to bottom): nitrite, nitrate, silicic acid, and phosphate (all in μM). This section crosses the shelf break and occupied the prominent glacial trough, as shown in Figure 2.

B) Example cross section of integrated (top 50 m) macronutrient and algal pigment concentrations from the Nuuk grid (from CTD 8 to CTD 10, see Figure 2). i) Integrated macronutrients; ii) Integrated pigment concentrations. Error bars show propagated errors on integration calculation ($\pm 1\text{SD}$).

326 increase in Si:N. Integrated Chl *a* increased towards shore, indicative that at least some of
 327 the macronutrient decrease is a result of biological uptake into biomass. However, the ratio
 328 of Chl *a*:Chl *c* peaked at the shelf break, and then decreased again towards shore, indicating
 329 a lower diatom proportional contribution to biomass in the same locations as the lowest
 330 integrated water column DSi (Figure 3b, see also Appendix C).

331

332 3.1.2. Diatom productivity

333 Surface bSiO₂ production among the three sampling regions ranged from 0.05 – 0.31
 334 μmol Si L⁻¹ d⁻¹ (Figure 4). For the most part, rates declined with depth; however, the Orphan
 335 Knoll site had subsurface maxima at the 20% isolume (~10-20 m) and base of the euphotic
 336 zone (i.e. 1% isolume, 20-50 m). The production rates of bSiO₂ among the Nuuk profiles
 337 were typically higher than Orphan Knoll and Southern Greenland (Figure 4); however,
 338 samples incubated in the dark (collected from below the euphotic zone) in Nuuk still had
 339 measurable production.

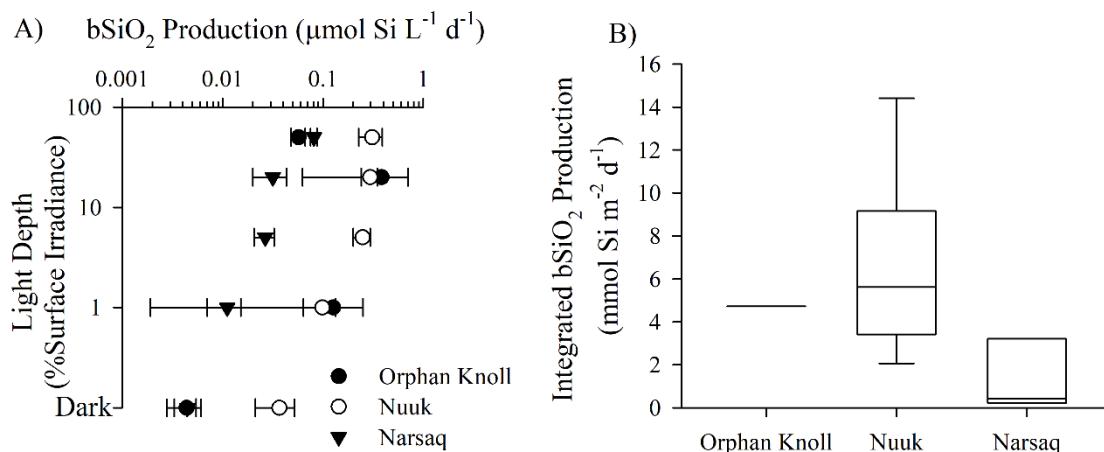


Figure 4: Biogenic silica (*bSiO₂*) production during ICYLAB. A) Averaged ($\pm 1SD$) gross rates of *bSiO₂* production ($\mu\text{mol Si L}^{-1} \text{d}^{-1}$) versus relative light depth (i.e. 100% is surface, 1% is base of the euphotic zone) among profiles within Orphan Knoll (filled circles), Nuuk (open circles), and Narsaq (filled triangles). B) Box plots of euphotic-zone integrated *bSiO₂* production ($\text{mmol Si m}^{-2} \text{d}^{-1}$) for profiles in Orphan Knoll ($n = 2$), Nuuk ($n = 9$), and Narsaq ($n = 6$).

340

341

342 3.1.3. Sediment dissolved silicon profiles

343 Pore water DSi collected from the mega cores and the ROV push cores from the
 344 Labrador Sea and coastal Greenland during DY081 expedition range from 49–616 μM (Figure
 345 5). All cores generally show an initial increase in pore water DSi with core depth, indicating

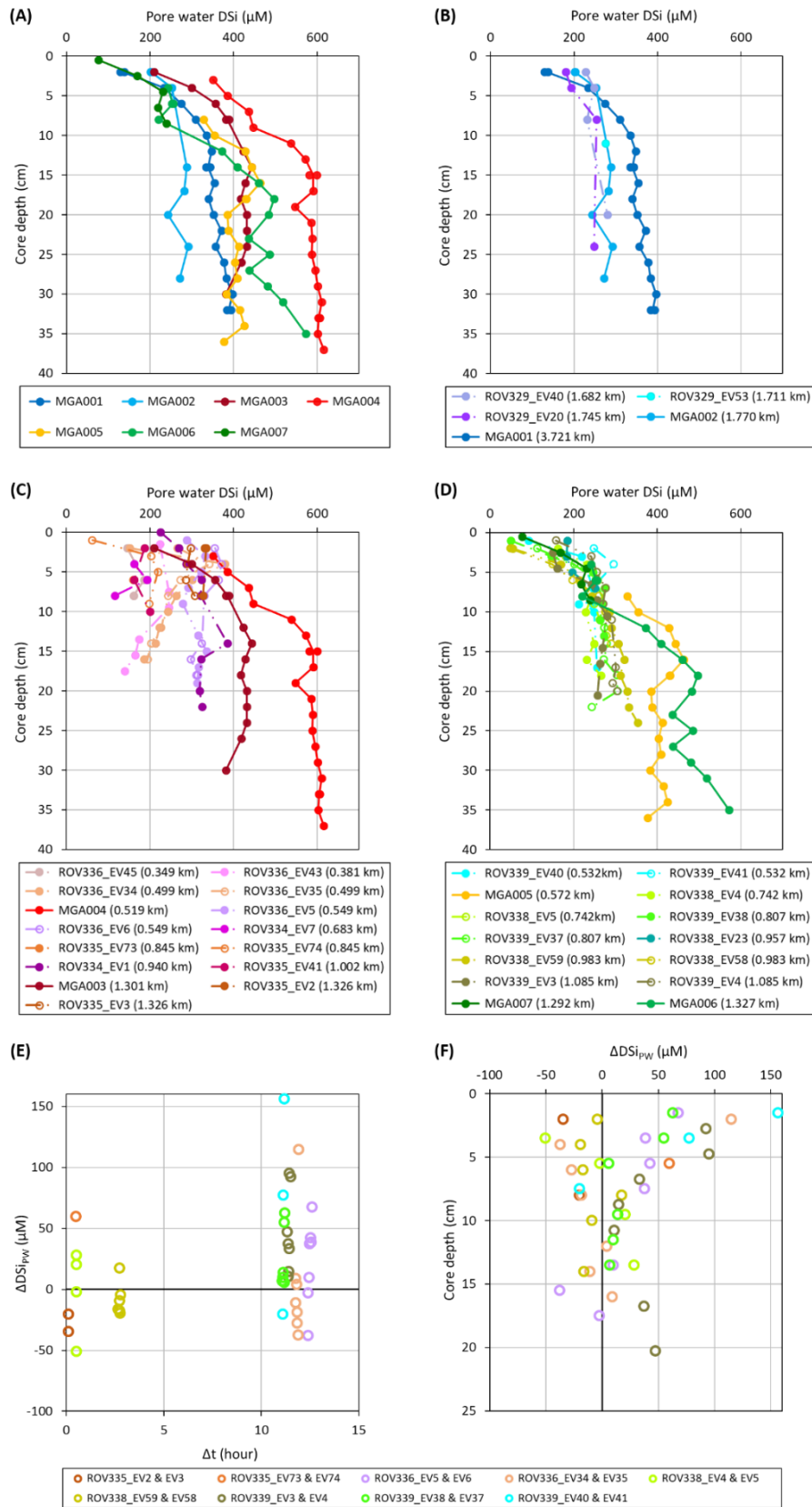


Figure 5: Pore water dissolved silicon concentration (DSi) measurements versus mega core (MGA, solid lines) or ROV push core (dash-dot lines) depths. Results from (a) mega cores, (b) Orphan Knoll cores, (c) cores off Nuuk, and (d) cores off Narsaq and Cape Farewell. Empty circles are results from replicate push cores retrieved at certain sites. Bracketed numbers in plot legends indicate water depths of the sediment cores.

Differences in pore water dissolved silicon concentration between replicate push cores that were sampled at different time periods (ΔDSiPW). ΔDSiPW was calculated by subtracting push core pore water DSi sampled at the latter time period from the corresponding replicate push core pore water DSi sampled at the earlier time period. The calculation was carried out between measurements from the same or nearby ($\leq \pm 1$ cm) sediment core depths. (e) ΔDSiPW versus the time difference between the sampling periods of the replicate cores (Δt), (f) ΔDSiPW versus core depth.

346 supply of Si to bottom waters from the sediment via dissolution. At greater depths, the rates
347 of increase of pore water DSi with depth slow down or even reverses (Figure 5).

348 There is good agreement between pore water DSi results (Figure 5) observed in ROV push
349 cores and mega cores from Orphan Knoll and South Greenland (off Narsaq and Cape
350 Farewell). To the best of our knowledge, this is the first formal comparison of pore water
351 DSi profiling using ROV push cores compared to megacorerers, and our results provide
352 confidence to the application of this sampling methodology in future studies, especially in
353 settings where the use of a megacorer proves to be challenging (e.g. complex bathymetry,
354 presence of coarse ice-rafted material). In contrast, there is larger variation in pore water
355 DSi (Figure 5) among the sites off Nuuk (Appendix C), which could in part be related to the
356 greater variability in sediment composition (e.g. ice-rafted debris, fossil fragments) and
357 characteristics (e.g. grain size) observed at these sites. More importantly, the highest pore
358 water DSi concentrations are observed (Figure 5) at the shallowest coastal site closest to
359 Nuuk (Appendix C), which is under the influence of meltwater from glacial fjords.

360 Replicate ROV push cores were collected at certain sites to evaluate any consistent
361 change in pore water DSi with time when the sediment cores were left standing onboard at
362 ambient temperature. Results show only minor discrepancies in pore water DSi: up to ± 60
363 μM when the sampling was carried out on paired replicate cores within 3 hours of each
364 other (Figure 5); this is likely due to spatial heterogeneity in sediments and pore waters. In
365 contrast, when pore water sampling was carried out on paired replicate cores more than 10
366 hours apart from each other, there are greater discrepancies with higher DSi values
367 measured in the pore water sampled later in time (Figure 5). Our results suggest that pore
368 water in the upper core depths might not reflect original DSi values if the sampling is carried
369 out more than 10 hours after retrieval of the sediment core.

370

371

372 **4. Discussion**

373 Our multi-disciplinary framework allows a nuanced understanding of the whole silica
374 cycle in this climatically critical region, and specifically, the impact of glacial meltwater in
375 shelf seas and into the open ocean. We are able to address questions surrounding the
376 amount of meltwater reaching the ocean, the mechanism by which it does so, and identify
377 mechanisms for how the meltwater is entrained in coastal and boundary currents. For the
378 main context of this study, we can then use this information to understand better the
379 implications of meltwater inputs on macronutrient distributions and biological production,
380 in particular the supply and uptake of DSi. Lastly, we use our palaeoclimate archives to
381 interrogate past changes in meltwater supplies, which are likely to have had a major impact
382 on nutrient cycling.

383

384 **4.1. Bathymetric features and their role in shelf-water dynamics**

385 The shipboard bathymetric and backscatter data provided a rapid insight into the
386 geomorphology of the study regions. The bathymetry features, resulting from their glacial
387 history, are likely to be an important influence on modern shelf-water dynamics and
388 biogeochemical cycling. The bathymetric grids obtained off the W Greenland coast include
389 the dedicated surveys offshore Nuuk, Narsaq and Cape Farewell, in addition to data
390 collected along the transits (Figure 6). They illustrate a wealth of geomorphological features
391 typical of glaciated margins, such as cross-shelf troughs, iceberg ploughmarks, gully systems,
392 submarine canyons and submarine landslides (Dowdeswell, Canals, Jakobsson, Todd,
393 Dowdeswell et al., 2016). Most notably off Nuuk, the inshore-deepening Gothåb (Nuuk)
394 Trough, previously described by Ryan, Dowdeswell and Hogan (2016), is likely to be
395 important in driving instabilities in localised circulation, influencing the mixing of melt and
396 glacially derived material into the shelf waters. The trough harbours a number of drumlins,
397 elongated features typical of glacial weathering, in addition to intricate patterns of iceberg
398 ploughmarks at the shallow trough mouth (Figure 6). Systems of gullies and submarine
399 canyons can be found at both the Gothåb and Narsaq trough-mouth fans, and along the
400 shelf edge (Figure 6). Some of the canyons are cut up to 350 m into the continental slope,
401 and feature steep to near-vertical walls along their flanks together with scoured channels at
402 their floors. Offshore Narsaq, some of the submarine canyons appear to have evolved as a
403 result of retrogressive failures cutting upslope along gullies (Figure 6).

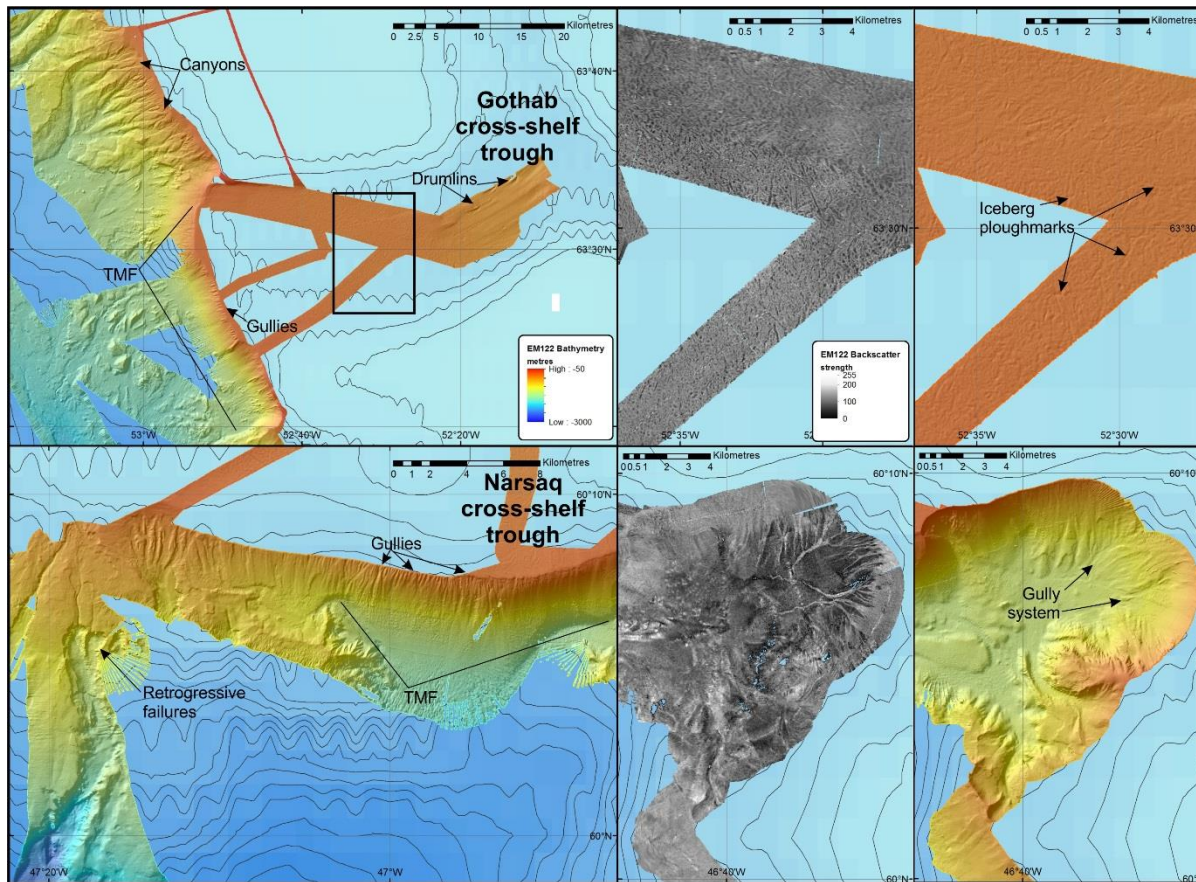


Figure 6: Examples of submarine glacial landforms offshore W Greenland identified in the shipboard multibeam data. Background: bathymetry from ETOPO5 (www.ngdc.noaa.gov/mgg/global/etopo5.HTML), contour interval 100 m. Location of maps indicated on Fig. 1. TMF: trough-mouth fan.

405

406

407 4.2. Physical tracers of glacial meltwater inputs, mixing and advection

408 We can use the gridded hydrographic and geostrophic velocity fields to constrain the
 409 flow of water across the shelf break, focusing on the Gothåb (Nuuk) Trough CTD section
 410 (Figure 2b). The subsurface temperature minimum indicates the core of Polar Surface
 411 Water, whilst the subsurface temperature maximum is Irminger Water. The Irminger Water
 412 is present between 200 m and 700 m over the continental slope, with a core temperature of
 413 4.9°C. There are clear traces of this water mass in the trough also, where warm ($\theta > 4^\circ\text{C}$) and
 414 saline ($S > 34.7$) water is observed near the bottom at CTD16 and CTD10. The Polar Surface
 415 Water core is spread across the whole section at 50-150 m, with minimum temperatures
 416 recorded at the station furthest onshore (CTD16).

417 Geostrophic velocities were calculated by referencing the geostrophic shear to the
418 velocity field measured directly with a Lowered Acoustic Doppler Current Profiler (LADCP).
419 The LADCP velocity field was de-tided, by subtracting the barotropic tide solution obtained
420 from the Oregon State University (OSU) model (Egbert & Erofeeva, 2002). The resultant
421 geostrophic velocity field reveals two surface intensified current cores, one on each side of
422 the trough mouth (Figure 7). The offshore core is associated with a hydrographic front
423 around 15 km west of the shelf break and extends down beyond 400m depth. Its offshore
424 location is consistent with the long-term average position of the West Greenland Current
425 (Myers, Donnelly & Ribergaard, 2009).

426 The inshore velocity core has a less distinct hydrographic signature and therefore its
427 origin is more uncertain at present. One possibility is that the velocity maximum is the result
428 of topographic steering of the inshore portion of the West Greenland Current by the
429 bathymetric trough. Alternatively, it could represent an eddy of offshore water that has
430 detached from the boundary current. A velocity maximum was also detected in a
431 bathymetric trough inshore of Fylla Bank (near Nuuk) in a numerical model simulation
432 (Myers et al., 2009), but there has been no further study into the nature of this feature to
433 date. Such strong inshore current anomalies have significant consequences for the transport
434 of terrestrially-derived freshwater and nutrients.

435 In addition to the mean flows, eddies formed from the West Greenland Current
436 transport water from the boundary current to the interior Labrador Sea, where they
437 contribute to the process of Labrador Sea Water formation (Katsman, Spall & Pickart, 2004).
438 Baroclinic instability is thought to be a key formation mechanism, and years of enhanced
439 baroclinicity tend to coincide with high eddy activity (Rykova, Straneo & Bower, 2015),
440 which transfer hydrographic anomalies into the interior. There is significant baroclinicity in
441 both branches of the WGC in our section, implying that eddy generation may be significant.
442 In addition, wind driven Ekman transport is likely to be a key driver in the export of shelf
443 water across the WGC and into the Labrador Sea interior (Schulze & Frajka-Williams, 2018).

444 Cuny, Rhines, Niiler and Bacon (2002) have suggested that, around this location, the
445 West Greenland Current splits into westward and northward flowing components. However,
446 the location of the splitting, and the partitioning of the water masses involved is not well
447 understood. There are two westward components that flow around the northern perimeter
448 of the Labrador Sea and a northward branch that extends close to the Greenland shelf break

449 (Cuny et al., 2002). Hydrographic signatures of the West Greenland Current have been
 450 reported near Greenland to the north, in the vicinity of Davis Strait and Baffin Bay (Cuny,
 451 Rhines & Kwok, 2005; Myers et al., 2009).
 452

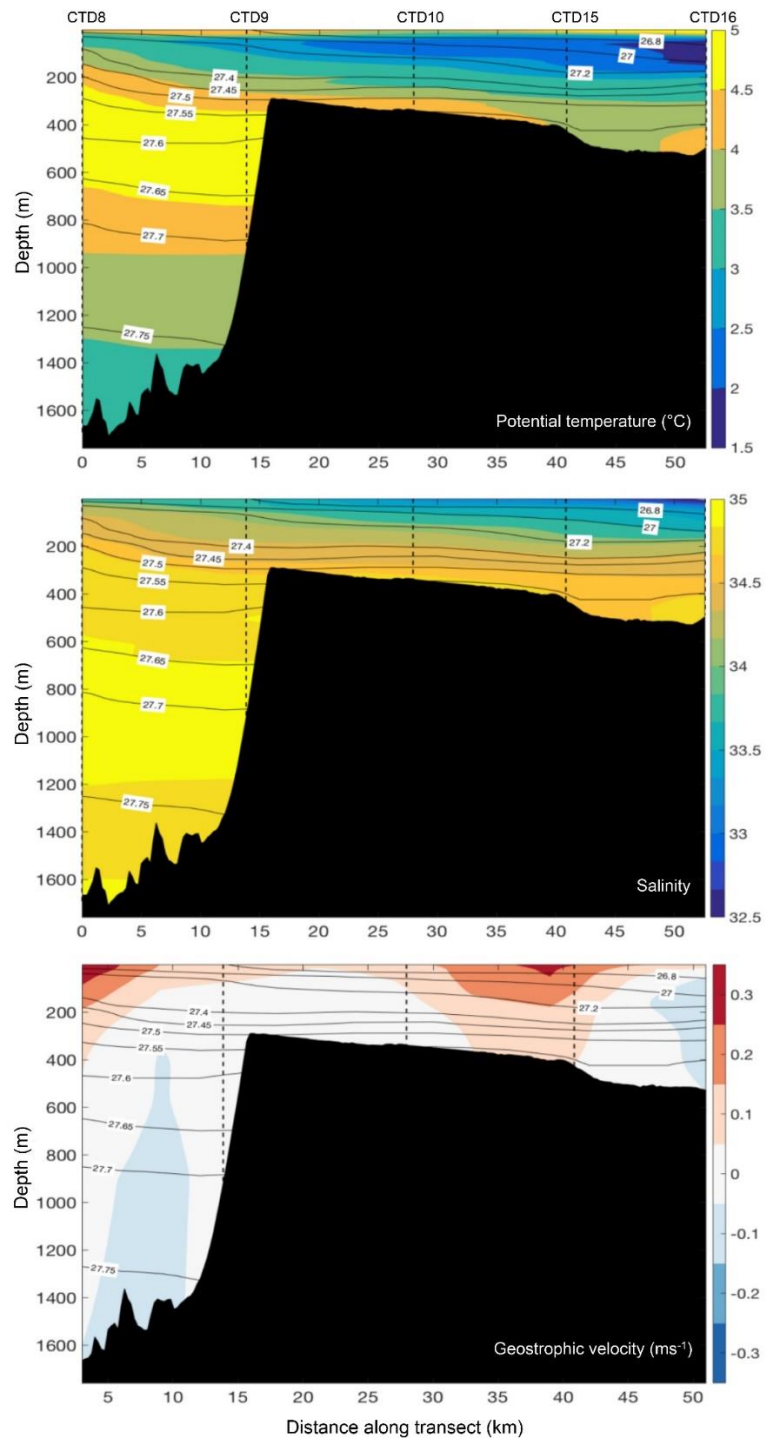


Figure 7: Gridded vertical sections, from top to bottom, of potential temperature ($^{\circ}\text{C}$), salinity, and geostrophic velocity (m s^{-1}) along Gothåb (Nuuk) Trough. The direction of geostrophic flow is perpendicular to the CTD section (positive northward and negative southward). The black lines with the white boxed labels are isopycnals, which are lines of constant potential density (in kg m^{-3}). The dashed vertical lines indicate the CTD stations, labelled at the top of each panel, from which these vertical sections were derived.

453

454 4.3. Chemical tracers of glacial inputs

455 4.3.1. Chemical tracers of meltwater

456 Vertical sections of sea ice melt and meteoric percentages based on seawater salinity
457 and $\delta^{18}\text{O}$ for the Gothåb (Nuuk) Trough CTD section (Figure 8), reveals a negative offshore
458 gradient in both sea ice melt and meteoric water percentages. Higher freshwater
459 concentrations are found in the trough at all depths, highlighting the potential for glacially-
460 sourced waters to reach the outer shelf and the strong boundary currents.

461 Freshwater mass balance calculations have, alternatively, been carried out in the High
462 Arctic using salinity and alkalinity endmembers resulting in robust meteoric water
463 percentage reconstructions (e.g. Hendry et al., 2018; Jones, Anderson, Jutterström & Swift,
464 2008). We compared the two mass balance methods using DY081 data, using both a high
465 meteoric water alkalinity endmember typical of the riverine input to the Arctic Ocean (Jones
466 et al., 2008), and a lower meteoric water alkalinity endmember typical of glacial meltwater
467 (Meire, Sjøgaard, Mortensen, Meysman, Soetaert et al., 2015). Our comparison indicates
468 that – irrespective of the endmember values chosen - alkalinity-derived values of meteoric
469 water percentages are impacted by subsurface processes that show correlations with nitrite
470 concentrations and temperature (Appendix C). Such non-conservative behaviour likely arises
471 as a result of enhanced alkalinity flux due to water column nitrification, and/or sedimentary
472 denitrification (Fennel, Wilkin, Previdi & Najjar, 2008; Wolf-Gladrow, Zeebe, Klaas,
473 Körtzinger & Dickson, 2007).

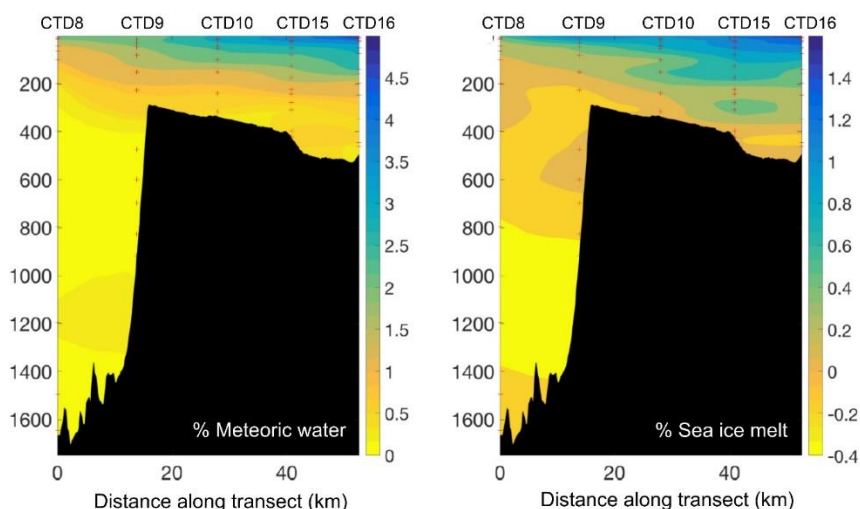


Figure 8: Vertical sections of meteoric water and sea ice melt percentages along Gothåb (Nuuk) Trough. The black area is the bathymetry of the section, as measured by the ship multibeam. Red pluses indicate the bottle sampling locations, with the CTD stations annotated above.

474

475

476 4.3.2. Geochemical tracers of particulate flux

477 Radium (Ra) is produced continuously from lithogenic material by the decay of thorium
478 (Th) and thus displays elevated concentrations near any sediment-water interface. Short-
479 lived Ra activities did not show a clear relationship with salinity (Figure 9), but did exhibit
480 informative regional variability. The relatively low activities around Cape Farewell indicate a
481 lack of recent lithogenic input upstream of this region (along the eastern coast of
482 Greenland). From Cape Farewell $^{224}\text{Ra}_{\text{XS}}$ increases westwards to $\sim 51^\circ \text{W}$, consistent with
483 increasing cumulative sedimentary inputs into the Greenland coastal current (Figure 9C). As

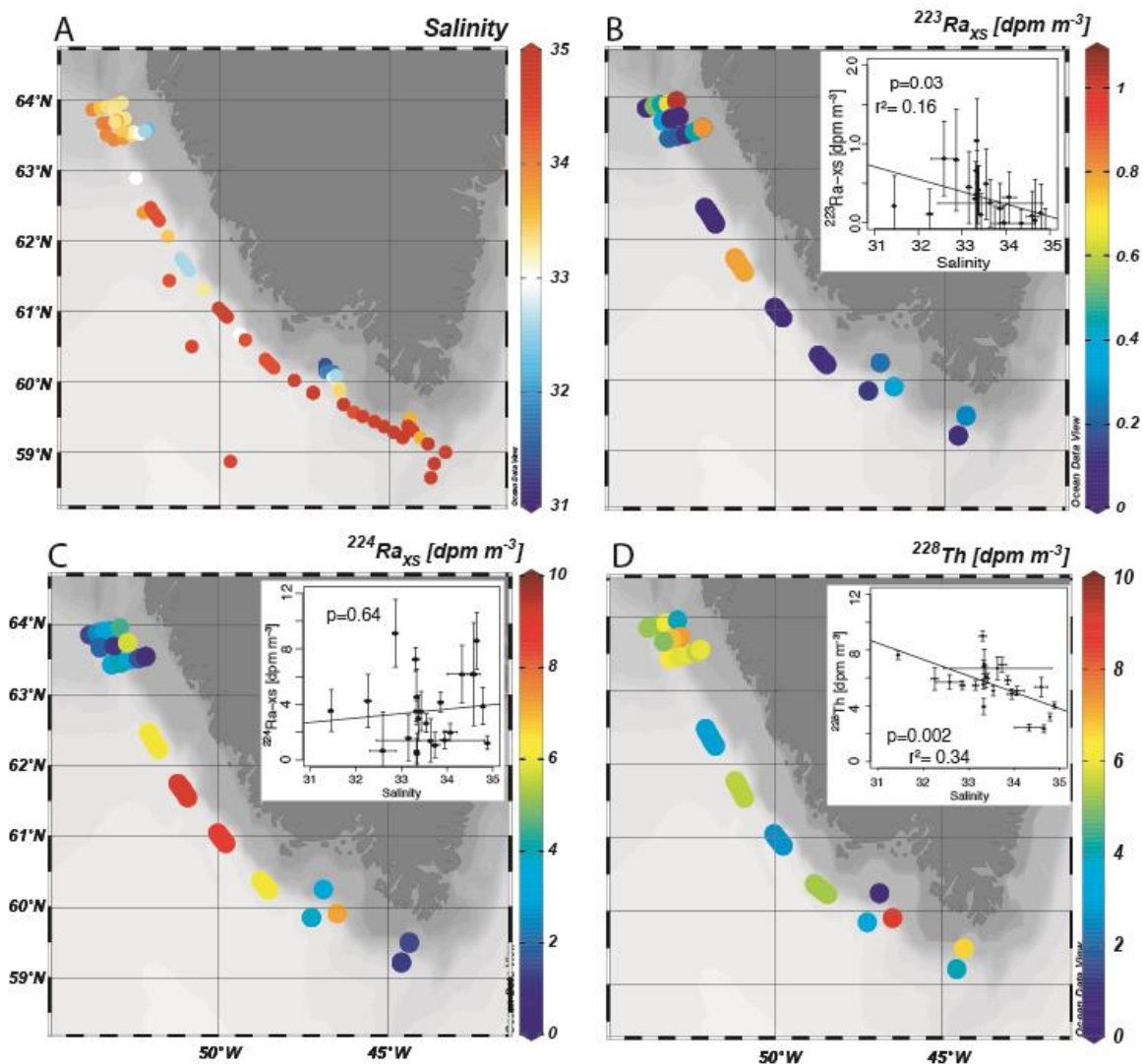


Figure 9: Spatial distribution of salinity (A), $^{223}\text{Ra}_{\text{XS}}$ (B) $^{224}\text{Ra}_{\text{XS}}$ (C) and ^{228}Th (D) from towfish samples taken at 2-5 m depth. Elongated symbols show underway samples which took $\sim 1\text{h}$ to collect. For B-D, inset plots show the same isotope versus salinity in surface waters. Vertical error bars denote ± 1 standard error for activities, and horizontal error bars show the standard deviation of salinity measurements taken each minute during the $\sim 1\text{ h}$ sampling interval.

484 CTD profiles show that the shallow surface mixed layer sampled by our towfish extended to
485 only 10-20 m, the most likely sources for $^{224}\text{Ra}_{\text{XS}}$ are glacial meltwater, very shallow
486 sediments within fjords, or resuspended shelf sediments by storm-driven mixing. This signal
487 then decreases towards Nuuk, which will reflect both dilution due to mixing and decay of
488 the short-lived isotope (half-life 3.66 d), and also suggests minimal further lithogenic input
489 into the surface mixed layer. The difference in activity from $\sim 9 \text{ dpm m}^{-3}$ at $\sim 51^\circ \text{ W}$ to < 4.5
490 dpm m^{-3} at the Nuuk sampling stations suggests a decay time of one half-life between these
491 sampling regions, a distance of 300-400 km, although dilution or additional inputs would
492 also affect the measured activity and cannot be fully quantified at present. However, the
493 maximum $^{224}\text{Ra}_{\text{XS}}$ activities of 8-9 dpm m^{-3} above deep water off the shelf break
494 demonstrate that this lithogenic signal is persistent, with the potential to rapidly transport
495 other glacial and sedimentary-derived compounds far offshore.

496 Although this spatial pattern is not clear in the longer-lived $^{223}\text{Ra}_{\text{XS}}$ (Figure 9B), the lower
497 overall activity of this isotope - as well as lower detection efficiency - lead to lower signal to
498 noise ratios. It is also likely that regional lithologies may lead to different input patterns due
499 to differing distribution of the ^{227}Ac and ^{228}Th parents.

500 Our analysis also quantifies ^{228}Th , the parent of ^{224}Ra . Due to its lithogenic origin and
501 higher particle reactivity, trends in ^{228}Th may be more closely associated with particulate
502 phases than Ra, especially in our unfiltered samples. Samples collected on fibre are
503 generally assumed to retain the majority of both particulate and dissolved Th, although in
504 coastal waters this approach may underestimate total ^{228}Th where particles can be flushed
505 through the sample, and the activities presented here also include supported activity from
506 ^{228}Ra (the parent of ^{228}Th) within the water column. Nevertheless, our ^{228}Th data (Figure 9D)
507 shows a statistically significant correlation with salinity. We therefore suggest that
508 contrasting patterns in the $^{224}\text{Ra}_{\text{XS}}$ daughter may be attributed to additional inputs from
509 fjord or shallow shelf sediments, as these inputs are more significant for dissolved species.
510 Additional samples from inner fjord locations and depths below the mixed layer will enable
511 us to differentiate between inputs from marine and glacial sediments.

512

513 **4.4. Diatom productivity in glacially-influenced shelf seas**

514 Despite the low nutrient concentrations, bSiO_2 production rates were significant in the
515 meltwater influenced waters off the shelf and slope. Similar surface DSi concentrations are

516 observed in the open-ocean gyres (e.g. North Pacific, Brzezinski, Krause, Church, Karl, Li et
517 al. (2011); North Atlantic, Krause, Nelson and Lomas (2010)) and typically do not support
518 high rates of diatom productivity. Spring-season bSiO₂ production rates in Svalbard and the
519 Barents Sea (Krause, Duarte, Marquez, Assmy, Fernández-Méndez et al., 2018) and at the
520 MarineBasis Nuuk station in Godthaabsfjord (Krause, Schulz, Rowe, Dobbins, Winding et al.,
521 In review) were routinely lower than those quantified at Orphan Knoll or Nuuk. The active
522 production below the euphotic zone suggests either recently exported diatoms (e.g. from
523 surface waters within 1-2 days) or the presence of siliceous and active Rhizaria (Biard,
524 Krause, Stukel & Ohman, 2018; Biard, Stemmann, Picheral, Mayot, Vandromme et al., 2016).
525 Integrated bSiO₂ production rates in the euphotic zone ranged two orders of magnitude,
526 0.13 – 14.4 mmol Si m⁻² d⁻¹. Four of the six stations off Southern Greenland had integrated
527 rates <1 mmol Si m⁻² d⁻¹, similar to mid-ocean gyres (Brzezinski et al., 2011), whereas all
528 other profiles during the cruise exceeded 2 mmol Si m⁻² d⁻¹. These rates are on the lower
529 end for the Southern Ocean (1-93 mmol Si m⁻² d⁻¹, Nelson, Treguer, Brzezinski, Leynaert and
530 Queguiner (1995)) but are similar to Svalbard and the Barents Sea during spring (0.3–1.5
531 mmol Si m⁻² d⁻¹, Krause et al. 2018). Overall, diatom bSiO₂ production consumed 4%
532 (median) – 10% (average) of the euphotic zone DSi inventory daily. These data are the first
533 such reports for this region of the Labrador Sea and Greenland, and demonstrate a
534 surprisingly active diatom assemblage despite low nutrients, temperature, and biomass.

535

536 **4.5. Influence of glacial meltwaters in the open ocean: Si cycling as a case study**

537 Although glacial meltwaters exhibit elevated concentrations of some dissolved nutrients
538 and reactive phases (e.g. Hawkings et al., 2017), glacial fjords – the conduits between the
539 source of these nutrients and the open ocean – are characterised by complex physical,
540 chemical and biological processes and are highly variable in space and time (Hopwood,
541 Carroll, Browning, Meire, Mortensen et al., 2018). Despite the highly heterogeneous nature
542 of these environments, we can use the findings from DY081 to shed more light on the key
543 common processes that characterise the transfer of nutrients across the land-ocean
544 interface, which will likely vary in rates and importance between different glaciated regions.

545 In many high-latitude regions, upwelled waters are thought to dominate the supply of
546 nutrients to the euphotic zone supporting most of the primary production. For example, off
547 the West Antarctic Peninsula (WAP), biological “hotspots” were thought to be fed by

548 upwelling Circumpolar Deep Water (CDW) being channelled onto the shelf via glacially
549 carved canyons (Schofield, Ducklow, Bernard, Doney, Patterson-Fraser et al., 2013).
550 However, there is increasing evidence that CDW is heavily modified as it transits onto the
551 shelf likely due to a flux of silica and iron from shallow marine sediments (Henley et al.,
552 2018; Sherrell et al., 2018). However, even in these relatively nutrient-rich environments,
553 there is still some important direct input from glacial meltwaters (e.g. Annett, Skiba, Henley,
554 Venables, Meredith et al., 2015) due to the release of reactive phases and promotion of
555 biological mediation of nutrient cycling through the formation of organic matter and
556 biogenic minerals.

557 Despite different boundary conditions compared to the WAP, similar processes are likely
558 to be happening in glaciated regions of SW Greenland. For example, elevated DSi (>20 μM)
559 in Greenlandic fjords measured in surface waters (Hawkings et al., 2017) cannot simply be
560 explained by mixing between the freshwater and marine end-members: these
561 concentrations are higher than the freshwater endmember, and there are no seawater
562 masses with sufficiently high DSi concentrations in the top 100m to supply this flux (Figure
563 3, see also Appendix C). The fjord water must be modified – in an analogous way to the WAP
564 – likely by particle-water interactions, including the release of DSi from reactive phases
565 derived from glacial weathering products, or biogenic silica (Hawkings et al., 2018; Hawkings
566 et al., 2017; Meire et al., 2016). This modification may be active in the water column, as well
567 as at the sediment-water interface, in the fjords as well as in the shallow water shelf-
568 sediments (Figure 5).

569 However, despite this enrichment within the fjord, the low-salinity waters reaching the
570 coastal ocean are low in DSi as a result of uptake mechanisms that are active as the fjordic
571 waters reach the shelf; our forthcoming studies of uptake kinetics and algal physiology from
572 within the fjords themselves will elucidate whether biological uptake is playing a key role in
573 Si cycling in these regions. Although there is apparently a limited supply of DSi exported
574 from fjords, there appears to be active cycling of silica by diatoms in coastal waters. Our
575 findings show the potential for meteoric waters, and glacially-derived particles, to be
576 exported as far as the coastal and boundary currents, and into the open ocean, where
577 further processing could act to release bioavailable elements. Whilst some of these
578 exported particles may dissolve within the water column during sinking, some will reach the
579 sediment-water interface. Pore water DSi can be used to evaluate the chemical changes of

580 the sediments post-deposition such as the dissolution of this reactive glacial material in
581 addition to dissolution of biogenic silica remains of diatoms and sponges, secondary or
582 'reverse' weathering, and the recycling of DSi back to the bottom waters (Rahman, Aller &
583 Cochran, 2017). The high, but variable, DSi concentrations found in the pore waters at our
584 coastal study sites point towards high rates of benthic regeneration fluxes. Calculated
585 sedimentary diffusive fluxes off SW Greenland, using the approach of Ragueneau, Gallinari,
586 Corrin, Grandel, Hall et al. (2001), range from 0.1-0.3 mmol Si m⁻² d⁻¹, and are at least 10% of
587 the diatom production rates. Our findings suggest that the total DSi flux across the
588 sediment-water interface, including from advective processes, could rival the magnitude of
589 water column biogenic silica production rates. The high uptake rates of diatoms, together
590 with this rapid recirculation of DSi across the sediment-water interface, points towards a
591 silica cycle maintained by strong pelagic-benthic coupling.

592

593 **4.5. Approaches to reconstructing glacial meltwater inputs through time**

594 Glacial meltwaters are enriched in both dissolved and particulate nutrients, including
595 silicon, and our new data highlight that these meltwaters extend across the shelf into
596 boundary currents. In the context of the marine silicon cycle, our data show that, whilst DSi
597 reaching the shelf waters from the glacial fjords may be low, diatom activity is surprisingly
598 high. DSi must be reaching the surface, potentially by mixing with modified shelf waters. Our
599 Ra isotopic data (section 4.3.2.) reveal that there is input of glacial particles into these shelf
600 waters, potentially via sediment reworking, which may contribute bioavailable silicon via
601 dissolution both in the water column and at the sediment-water interface. This system is
602 likely to be sensitive to glacial inputs, and so quantifying changes in meltwater fluxes
603 through time - using a variety of climate archives - is going to be key to understanding shelf
604 and slope productivity during past episodes of climatic change.

605

606 *4.5.1. Fossil deep-sea corals*

607 The geochemistry of fossil skeletons of deep-sea corals has the potential to record
608 aspect of past environmental conditions (Chen, Robinson, Beasley, Claxton, Andersen et al.,
609 2016; Robinson, Adkins, Frank, Gagnon, Prouty et al., 2014). In particular, water masses
610 distribution and food supply are thought to be important for deep-sea coral populations off
611 the West Greenland margin. Given their environmental sensitivity, cold-water coral

612 distributions are likely to be susceptible to changes in water mass properties and primary
613 production caused by meltwater inputs. In 2017, the first living samples of the cold-water
614 scleractinian coral, *Lophelia pertusa*, were collected from approximately 60° 22'N off the
615 Greenland within a layer of relatively warm, modified Atlantic Water (Kenchington,
616 Yashayaev, Tendal & Jørgensbye, 2017).

617 We have now been able to make in situ observations of cold water corals off
618 Greenland, as well as showing that corals have been present on the Greenland Margin for at
619 least 10,000 years (Figure 10). These first populations likely appeared with melting of the
620 large ice fields of the last glacial period. Supporting prior research, we also found that
621 scleractinian corals have been present further south on Orphan Knoll for at least 130,000
622 years (Figure 10; Cao, Fairbanks, Mortlock & Risk, 2007; Hillaire-Marcel, Maccali,
623 Ménabréaz, Ghaleb, Blénet et al., 2017). In both locations our suite of dates show that the
624 populations have not been stable. This observation implies shifts in environmental pressures
625 over these timescales, likely driven by a shift in balance between warmer Atlantic waters
626 and cold meltwater-rich polar waters.

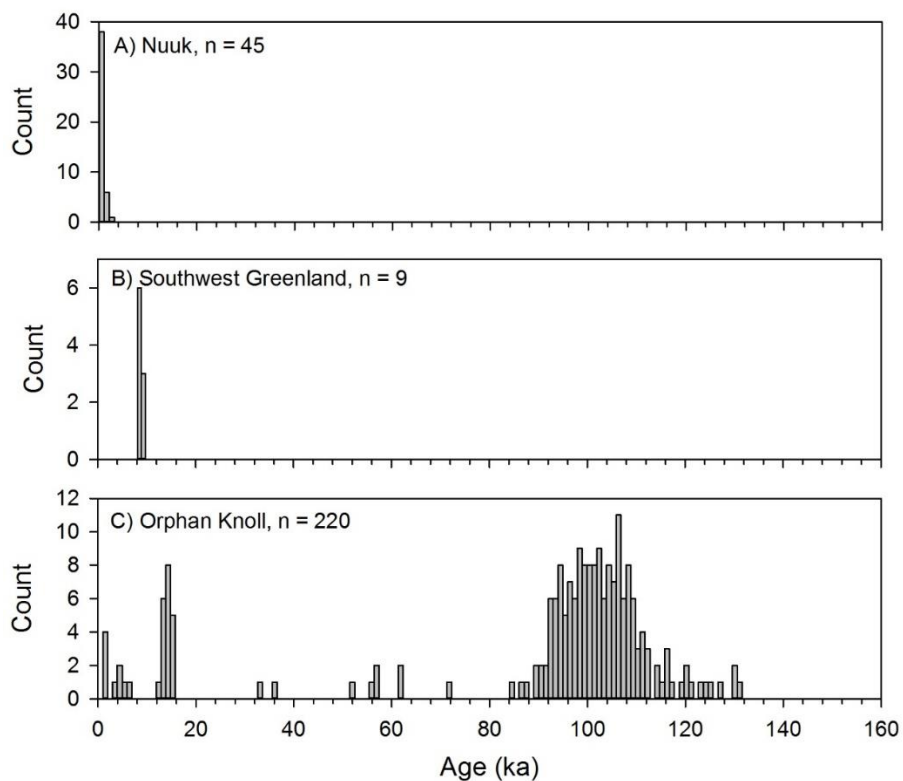


Figure 10: Uranium-thorium age data for fossil corals collected during DY081.

627

628 4.5.2. *Marine sediments and past glacial meltwater inputs*

629 During the last ice age, catastrophic iceberg discharge events episodically flooded the
630 subpolar North Atlantic with meltwater (Heinrich, 1988). Evidence suggests that these
631 “Heinrich events” (Broecker, Bond, Klas, Clark & McManus, 1992), were related to, and may
632 have acted as the trigger for (Broecker, 2003; Clark, Pisias, Stocker & Weaver, 2002),
633 dramatic changes in ocean circulation (McManus, Francois, Gherardi, Keigwin & Brown-
634 Leger, 2004) and heat distribution that were felt globally (e.g. Wang, Cheng, Edwards, An,
635 Wu et al., 2001). In addition to global impacts, changes in ice sheet dynamics and meltwater
636 inputs would also have had considerable impacts on more regional biogeochemical cycling.
637 While previous work has identified the existence of eight such events over the last 70 ka
638 (Andrews, Jennings, Kerwin, Kirby, Manley et al., 1995; Bond, Heinrich, Broecker, Labeyrie,
639 McManus et al., 1992; Bond & Lotti, 1995; Rashid, Hesse & Piper, 2003; Stoner, Channell &
640 Hillaire-Marcel, 1996), questions remain about the origin(s) of these events, their trigger(s)
641 and the nature of their primary signatures across the North Atlantic (Andrews & Voelker,
642 2018). Gravity cores collected at Orphan Knoll (DY081-GVY002 & GVY002), Southwest
643 Greenland (DY081-GVY003) and Cape Farewell (DY081-GVY004 & GVY 005) represent new
644 opportunities to constrain the timing, geometry and character of iceberg discharge and
645 glacial meltwater release in the paleo record.

646 Existing work on marine sediment cores from the high latitude North Atlantic has
647 employed a variety of proxies to identify pulses of meltwater delivery and associated ice
648 rafted debris delivery. Previously applied proxies include $^{230}\text{Th}_{\text{xs},0}$ (to assess changes in
649 sedimentary fluxes (McManus, Anderson, Broecker, Fleisher & Higgins, 1998)), counts of IRD
650 and foraminifera (to identify the relative abundance of terrestrially-derived debris and
651 foraminifera (Heinrich, 1988)), foraminifera census (to determine the relative abundance of
652 cold-dwelling planktonic species such as *N. pachyderma s.* (Ruddiman, Sancetta &
653 McIntyre, 1977)), $\delta^{18}\text{O}$ of *N. pachyderma s.* (to quantify the cooling and/or freshening of
654 surface waters (Bond, Broecker, Johnsen, McManus, Labeyrie et al., 1993)), magnetic
655 susceptibility (to identify detrital sediment (Grousset, Labeyrie, Sinko, Cremer, Bond et al.,
656 1993)), x-ray diffraction (XRD) (to assess changes in the abundance of quartz and plagioclase
657 feldspar (Moros, Kuijpers, Snowball, Lassen, Bäckström et al., 2002; Moros, McManus,
658 Rasmussen, Kuijpers, Dokken et al., 2004)), and X-ray fluorescence (XRF) (to identify changes
659 in sedimentary elemental ratios (Hodell, Channell, Curtis, Romero & Röhl, 2008)).

660 Unfortunately, the comparison of sediment core records has been limited by difficulties in
 661 establishing tightly constrained chronologies. This has impeded analysis of the triggers of
 662 events and the range of their influence (Andrews & Voelker, 2018). While previous work has
 663 utilized one or more of the proxy approaches identified above, complete assessment of the
 664 proxies described above, in a single core, would greatly assist in interpreting the
 665 paleoceanographic record. In addition, despite the widespread inference that icebergs
 666 originated from the Laurentide ice sheet during these events (Bond & Lotti, 1995; Broecker,
 667 2003; Hodell et al., 2008; McManus et al., 1998), relatively fewer detailed studies have
 668 examined their imprint and consequences in the proximal Labrador Sea (Andrews &
 669 Voelker, 2018).

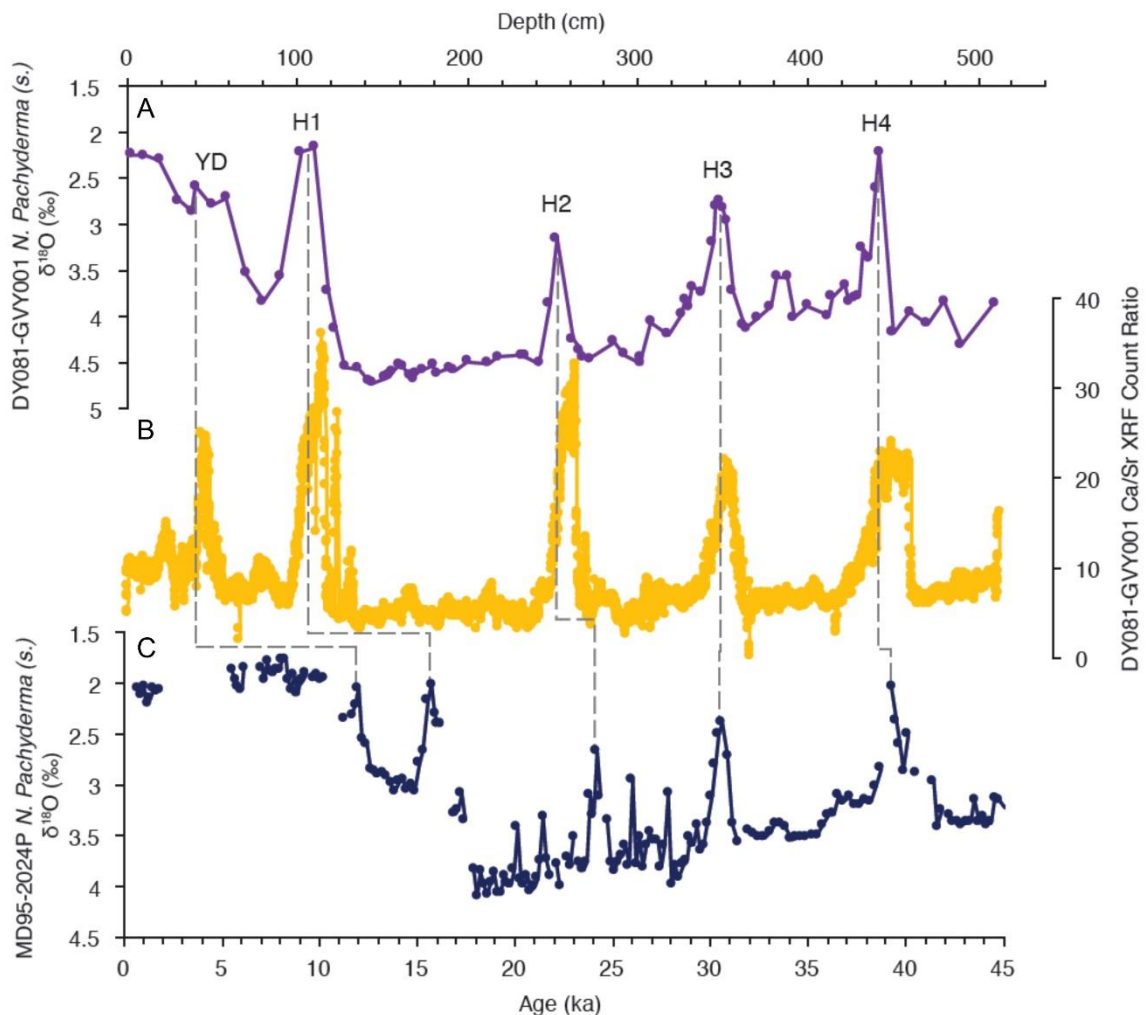


Figure 11: Proxies for North Atlantic Heinrich Events. a) *N. Pachyderma* (s.) $\delta^{18}\text{O}$ from DY081-GVY001 (purple). b) Ca/Sr XRF count ratio from DY081-GVY001 (yellow). c) *N. Pachyderma* (s.) $\delta^{18}\text{O}$ (Hillaire-Marcel & Bilodeau, 2000) on the age model of Lynch-Stieglitz, Schmidt, Henry, Curry, Skinner et al. (2014) (navy blue). Vertical grey dashes suggest age-depth assignments for DY081-GVY001.

670

671 Our goal in analysing the new DY081 cores is to use a wide range of proxies to address
672 temporal relationships and the spatial signatures of Heinrich events. Our findings show that
673 GVY001 (Orphan Knoll) represents a record of continuous sedimentation from 40-50 ka to
674 present and likely captures the Younger Dryas and Heinrich events 1-4 (Figure 11). In
675 GVY001 Heinrich event signatures have been identified in records of IRD counts, the $\delta^{18}\text{O}$ of
676 planktonic foraminifera, XRD and XRF scans. These results confirm the utility of using the
677 suite of proxies in DY081 cores to tie together previously incomparable records from
678 sediment cores in which disparate proxies have been applied, to reconstruct meltwater
679 inputs in the region back through time.

680

681 **5. Synthesis and Outlook**

682 Coastal and shelf sea biogeochemical research in the polar regions requires high-
683 resolution spatial and temporal datasets, due to the inherent heterogeneous nature of the
684 high-latitude margin settings. Whilst obtaining the necessary temporal resolution is
685 challenging, especially in the absence of expensive long-term monitoring programs, it is
686 possible to combine traditional physical and biogeochemical measurements with novel
687 isotopic and observational methods that integrate signals over a variety of timescales (days
688 to thousands of years). Stable and radiometric isotope geochemistry also allows the
689 identification of common processes within this highly-variable system, which are active over
690 given timescales. All of these approaches can be combined with palaeoceanographic
691 techniques to obtain a reliable baseline for pre-industrial conditions, and also look for
692 analogues of future change from the past.

693 In the context of the marine silica cycle, our findings from DY081 are able to show that:

- 694 • There are strong mean flows that are conducive to eddy generation, which will likely
695 transport freshwater from the margin into the boundary currents that supply the
696 Labrador Sea;
- 697 • Oxygen isotopes robustly trace meteoric water composition adjacent to Greenland,
698 with near-surface concentrations of 5‰ over the shelf reflecting significant glacial
699 discharge;
- 700 • Ra isotopes indicate additions of glacial meltwater and sedimentary particulates are
701 spatially heterogeneous and rapidly transported;

- 702 • Low macronutrient concentrations (e.g. DSi) are found in coastal waters influenced
703 by glacial melt;
- 704 • Diatoms are surprisingly active given the low nutrient availability and low
705 temperature (i.e. consuming 5-10% of euphotic zone Si daily);
- 706 • There is a strong benthic flux of DSi from sediments;
- 707 • Fossil corals can be used to track changes in benthic ecosystems through time, likely
708 influenced by water mass distribution;
- 709 • Sediment cores recovered of sufficient length and resolution to reconstruct
710 meltwater inputs at least back to 45 ka (i.e. Heinrich events 0-4).

711

712 **Acknowledgments**

713 The authors would like to thank the Captain and crew of the RRS *Discovery*, the
714 National Marine Facility technicians, David Turner, and project manager, Daniel Comben,
715 National Oceanography Centre Southampton (NOCS). Many thanks to Sinhue Torres-Valdes
716 and Christopher D. Coath for assistance in the laboratory, and the Marine Geoscience group
717 at NOCS for providing the core-splitter. Funding for DY081 was from the European Research
718 Council (ERC Starting Grant 678371 ICY-LAB). The contributions of AWJ, GGC, and JFM were
719 supported in part by the US-NSF.

720

721

722

723 Table 1: End-member values used in the mass balance calculations.

	Irminger	Meteoric	Sea ice
Salinity	34.88	0	3
$\delta^{18}\text{O}$ (‰)	+0.34	c. -21	Surface values +2.1

724

725

726 **APPENDIX A: Oceanographic setting**

727

728 The strong West Greenland Current (WGC) brings cold Arctic Water (AW) around the
729 southern tip of Greenland and northwards into the Labrador Sea (Yang et al., 2016). The
730 Irminger Current (IC) brings in warmer North Atlantic Water (NAW) from the North Atlantic
731 into the Labrador Sea – this water is ultimately derived from the Gulf Stream. The typical
732 water column structure near coastal Western Greenland is stratified by salinity, comprising
733 cold, surface water (found shallower than approximately 100 m) that consists of AW and
734 additional meltwater, overlying a strong thermocline; NAW (temperature > 3°C, salinity <
735 34.5) is found below the thermocline, with the water temperature peaking at a depth of
736 approximately 400m, most likely representing the core of Irminger Water inflow (McCartney
737 and Talley, 1982).

738 At approximately 64 °N, the latitude of Nuuk, the WGC bifurcates into the Labrador
739 Current (LC), and a proportion is diverted into the interior of the Labrador Sea, where deep
740 water formation occurs by winter-time convection driven by oceanic heat loss (McCartney,
741 1992). The newly formed Labrador Sea Water (LSW) enters the North Atlantic as the Deep
742 Western Boundary Current, to form the upper layers of North Atlantic Deep Water (NADW),
743 which subsequently become the intermediate layers of the North Atlantic meridional
744 overturning circulation. By the time the boundary current reaches Orphan Knoll (Figure 2a),
745 sub-thermocline warm, saline waters are underlain by the LSW and overflow waters (likely
746 Gibbs Fracture Zone Water and Demark Strait Overflow Water) (Yang et al., 2016).

747

748

749

750 **APPENDIX B: Details of methodologies**

751 Full details of on-board methodology and approach can be found in the DY081 cruise
752 report (Hendry, 2017), but are summarised briefly here.

753

754 *B.1. Water column sampling and on-board processing: glacial meltwater inputs, nutrients,*
755 *and phytoplankton*

756 Water column samples were collected using Niskin bottles attached to the CTD
757 rosette (10L volume) and the Remotely Operated Vehicle (ROV) *Isis* (4 L volume), and via a
758 trace-metal clean towfish.

759 Duplicate samples for inorganic macronutrients were filtered using either an Acropak
760 or in-line polycarbonate filter (0.2 µm) into acid-cleaned and rinsed high density
761 polyethylene (HDPE) bottles and frozen immediately at -20°C. Clean handling techniques
762 were adopted and only Semperguard vinyl non-powdered gloves were used for the sample
763 handling. Samples for biogenic/amorphous silica were filtered through 25mm 0.6 µm
764 polycarbonate filters, dried and stored for analysis back on land.

765 Samples were also collected for water oxygen isotope composition ($\delta^{18}\text{O}$) and
766 carbonate chemistry parameters (pH, alkalinity), which are used for investigating freshwater
767 input in high-latitude regions (Hendry et al., 2018; Meredith et al., 2008; Thomas et al.,
768 2011). For $\delta^{18}\text{O}$, an unfiltered water sample was sealed tightly in a (rinsed) 60 mL HDPE
769 plastic bottle and stored in a cool, dark storage location. For carbonate chemistry, a 250 mL
770 borosilicate glass bottle was rinsed twice with seawater from the Niskin before being filled
771 using a PVC tube and allowed to overflow one volume; a glass stopper was placed in the
772 bottle neck to displace excess seawater then 2.5 mL of seawater was pipetted off to allow a
773 1% headspace. The sample was poisoned with 50 µL saturated mercuric chloride solution
774 and sealed, homogenised and stored in a cool, dark storage location.

775 Phytoplankton pigments were analysed on board, and compared to sensor-derived
776 fluorescence data, to assess algal standing stocks in relation to meltwater input. Seawater
777 was filtered using GF/F filters and then frozen at -20 °C until extraction. A trichromatic
778 method (Mackereth et al., 1978) was used to determine chlorophyll (Chl) a, b, and c
779 spectrophotometrically in the near surface seawater samples. Chlorophyll extraction was
780 carried out using aqueous acetone buffered with magnesium carbonate, for 24 hours in the
781 dark at 4°C. The samples were then centrifuged and analysed at 750 nm (to correct for
782 turbidity), 664 nm, 647 nm, and 630 nm on a V-1200 Vis spectrophotometer. Absorbance
783 values were then used in equations 1 to 3 to calculate the concentration of Chl *a*, *b*, and *c*
784 per volume of filtered sample (Eq. 4).

$$785 \text{Chl } a \text{ (mg/L)} = 11.85 * (\text{OD}_{664}) - 1.54 * (\text{OD}_{647}) - 0.08 * (\text{OD}_{630}) \quad (1)$$

$$786 \text{Chl } b \text{ (mg/L)} = 21.03 * (\text{OD}_{647}) - 5.43 * (\text{OD}_{664}) - 2.66 * (\text{OD}_{630}) \quad (2)$$

$$787 \text{Chl } c \text{ (mg/L)} = 24.52 * (\text{OD}_{630}) - 7.60 * (\text{OD}_{647}) - 1.67 * (\text{OD}_{664}) \quad (3)$$

$$788 \text{Chl } x, \text{ mg/m}^3 = (\text{Chl } x) * \text{extract volume, L} / \text{Volume of sample, m}^3 \quad (4)$$

789

790 *B.2. Additional laboratory techniques*

791 Seawater oxygen isotope ($\delta^{18}\text{O}$) measurements were made using the CO_2 equilibration
792 method with an Isoprime 100 mass spectrometer plus Aquaprep device at the British
793 Geological Survey (Keyworth). 200 μl samples of water were loaded into exetainers (3.7ml
794 Labco Ltd.) and placed in the heated sample tray at 40°C. The exetainers were then
795 evacuated to remove atmosphere, then flushed with CO_2 and left to equilibrate for between
796 12 (first sample) - 37 (last sample) hours. Each individual gas sample was then admitted to
797 the cryogenic water trap where any water vapour was removed. The dry sample gas was
798 then expanded into the dual inlet where it was measured on the transducer before being
799 expanded in the dual inlet bellows. Ionvantage software balanced the reference bellows
800 relative to its volume. The sample and reference CO_2 gases entered alternatively into the
801 Isoprime100 through the dual changeover valve for isotope ratio measurement. In each run
802 two laboratory standards (CA-HI and CA-LO) plus up to two secondary standards were
803 analysed in triplicate. The value of these laboratory standards has been accurately
804 determined by comparison with international calibration and reference materials
805 (VSMOW2, SLAP2 and GISP) and so the $^{18}\text{O}/^{16}\text{O}$ ratios (versus VSMOW2) of the unknown
806 samples can be calculated and are expressed in delta units, $\delta^{18}\text{O}$ (‰, parts per mille).
807 Isotope measurements used internal standards calibrated against the international
808 standards VSMOW2 and VSLAP2. Errors are typically $\pm 0.05\text{‰}$ for $\delta^{18}\text{O}$.

809 Carbonate analysis was carried out at GEOMAR, Germany. For Total Dissolved Inorganic
810 Carbon (TDIC), carbonate species were converted to CO_2 by addition of phosphoric acid
811 (10% in 0.7 M NaCl), this generated CO_2 is then carried into the measurement cell using N_2
812 and analysed by coulometric titration using a VINDTA 3C (Marianda, Germany) connected to
813 a 5011 coulometer (UIC, USA). For Total Alkalinity (TA) samples are titrated with 0.1 M HCl
814 (prepared in 0.7 M NaCl) in 150 μL increments until the carbonic acid equivalence point is
815 reached. The titration is monitored with the VINDTA 3C in a closed cell titration (Dickson et
816 al., 2007). Measurements were calibrated using certified reference material from Prof.
817 Dickson, Scripps. The temperature, salinity, and nutrient concentrations of the samples at
818 time of sampling are then combined with the TDIC and TA measurements to calculate CO_2
819 system parameters (pH and pCO_2).

820 Samples for inorganic nutrients were all analysed at the Plymouth Marine Laboratory
821 using the latest GO-SHIP (Hydes et al., 2010) recommended defrosting technique of heating

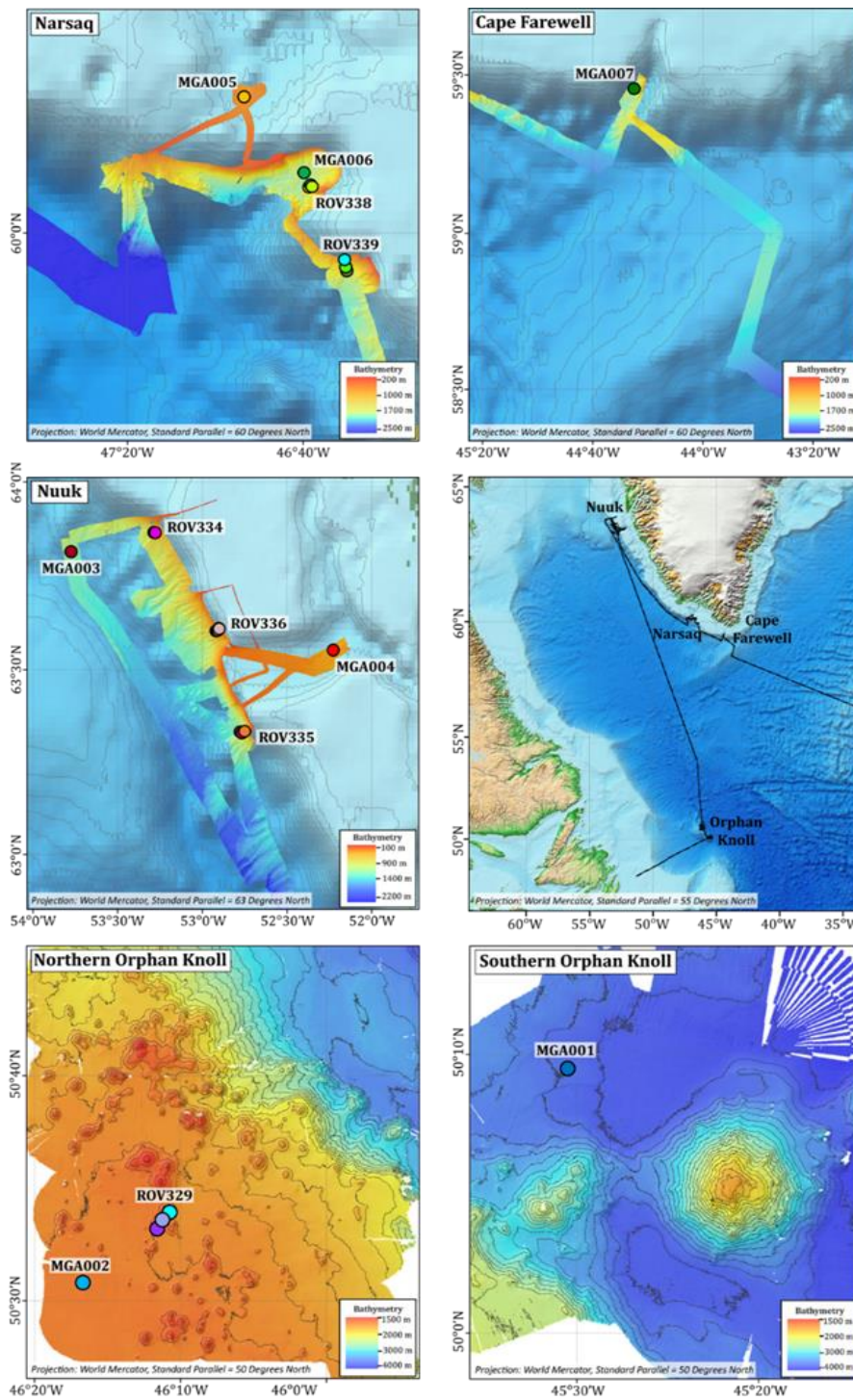
822 in a warm water bath for 45 minutes from frozen and then equilibrating to room
823 temperature for another 30 minutes before analysis. The analysis was carried out using a
824 SEAL analytical AAIII segmented flow colorimetric auto-analyser using classical analytical
825 techniques for nitrate, nitrite, silicic acid (or DSi) and phosphate, as described in Woodward
826 and Rees (2001). Clean sampling and handling techniques were employed during the
827 defrosting, sampling and manipulations within the laboratory, and where possible carried
828 out according to the International GO-SHIP nutrient manual recommendations of Hydes et
829 al. (2010). Seawater nutrient reference materials (KANSO Ltd. Japan) were also analysed to
830 check analyser performance and to guarantee the quality control of the final reported data.
831 The typical uncertainty of the analytical results were between 2-3%, and the limits of
832 detection for nitrate and phosphate were 0.02 μM , 0.01 μM for nitrite, and silicic acid did
833 not ever approach the limits of detection.

834 We dated 274 fossil scleractinian corals from the three main target sites (Orphan
835 Knoll, Nuuk, South Greenland) using a reconnaissance dating technique based on the decay
836 of uranium to thorium (Spooner et al 2015, Chen et al 2015).

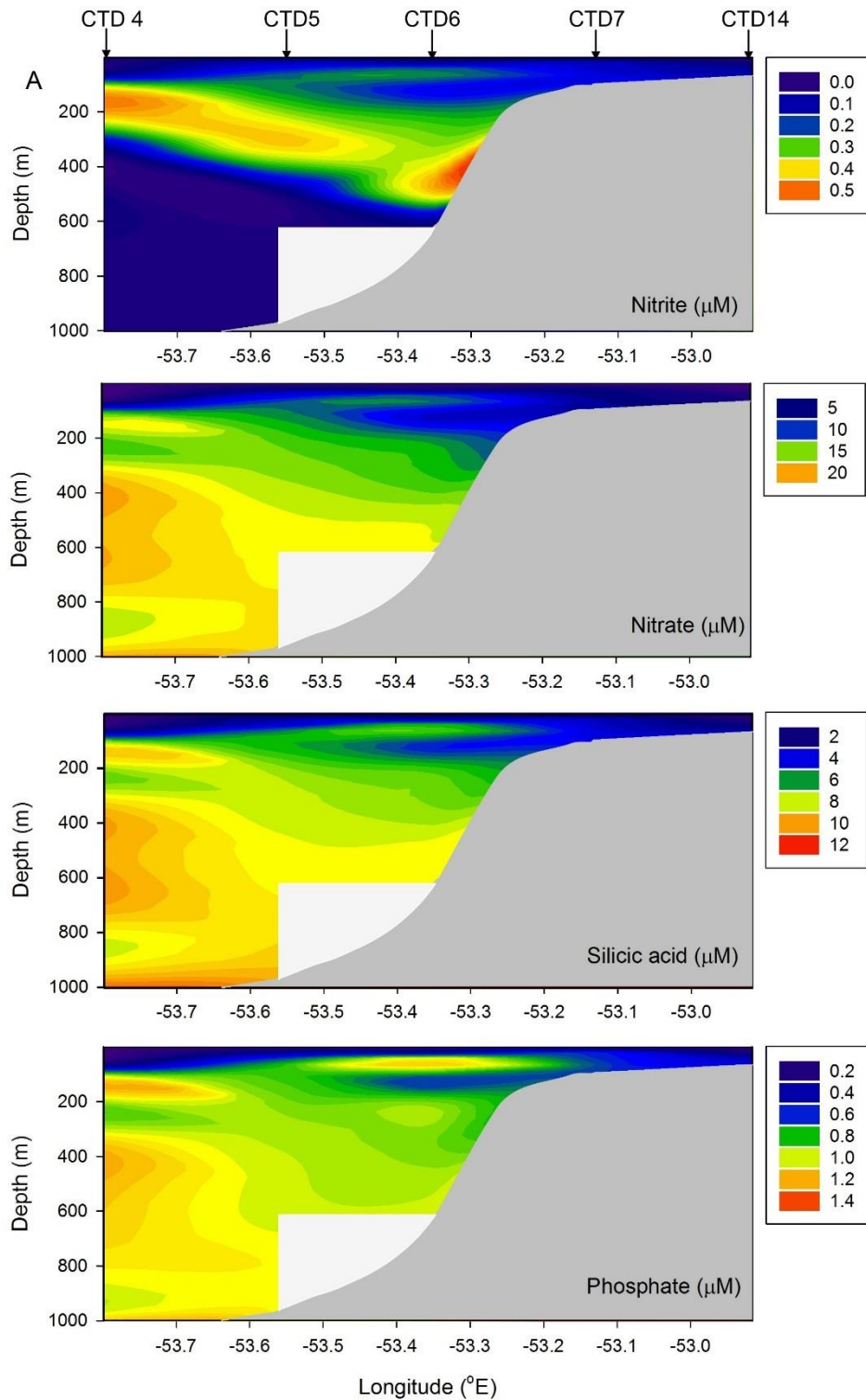
837 Foraminifera samples for stable isotope analysis were processed and analysed at the
838 Lamont-Doherty Earth Observatory of Columbia University. Samples were freeze-dried and
839 then washed through a 63 μm sieve and the >63 μm fraction dried at 45°C overnight. Five to
840 ten specimens of *Neogloboquadrina pachyderma* (sinistral) were picked from the >250 μm
841 size fraction, weighed to ensure consistent sample sizes and then analysed on a Thermo
842 Delta V Plus with Kiel IV individual acid bath device. Values were calibrated to the VPDB
843 isotope scale with NBS-19 and NBS-18. Reproducibility of the in-house standard (1SD) is
844 $\pm 0.06\text{‰}$ for $\delta^{18}\text{O}$ and $\pm 0.04\text{‰}$ $\delta^{13}\text{C}$.

845 Ca and Sr intensities (count rates) were measured with an x-ray fluorescence (XRF)
846 core scanner (ITRAX, Cox Ltd., Sweden) at the British Ocean Sediment Core Research Facility
847 (BOSCORF). Split core surfaces were smoothed and covered with polypropylene film to
848 minimize desiccation during analysis. Elemental counts were collected at 1 mm resolution,
849 using an integration time of 2s and a molybdenum x-ray source set to 30kV and 30mA.

850
851

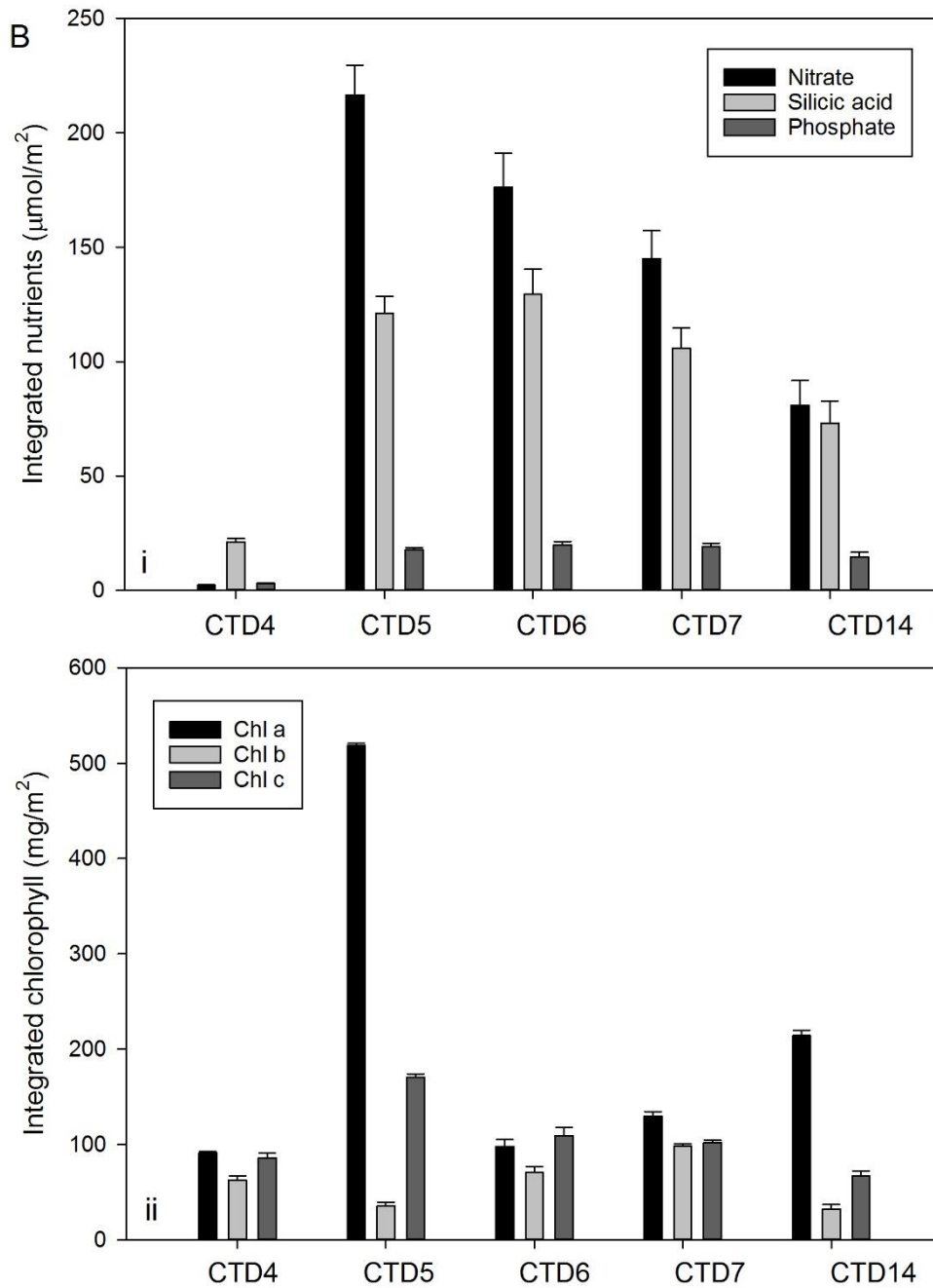


854
 855 Figure A1. Maps showing DY081 mega core (MGA) and ROV push core sites where pore-fluid
 856 samples were taken, and cruise track (black line). Bathymetry resolution of the sampling
 857 regions were improved with shipboard multibeam survey. Circles marking the core locations
 858 have the same colours corresponding to those denoting the core identities in Figure 5.
 859



860

861 Figure A2: A) Example cross section of macronutrient concentrations from the northern
 862 section of the Nuuk grid (from CTD 4,5,6,7,14, see Figure 2), showing (from top to bottom):
 863 nitrite, nitrate+nitrite, silicic acid, and phosphate (all in μM). This section encompasses the
 864 margin from the slope onto the shelf, and did not occupy the bathymetric trough (c.f. Figure
 865 3, main text).



867

868

869

870

871

872

873

B) Example cross section of integrated (top 50m) macronutrient and algal pigment concentrations from northern section of the Nuuk grid (from CTD 4 to CTD 7, 14, see Figure 2). i) Integrated macronutrients; ii) Integrated pigment concentrations. Error bars show propagated errors on integration calculation (1SD).

A. Calculation one

Salinities set as per $d^{18}O$ mass balance (see main text)

Meteoric water alkalinity = 1000

Seawater alkalinity = 2312

Sea-ice alkalinity = 175

(Alkalinity in $\mu\text{mol/kg}$;

Data from Jones et al., 2008)

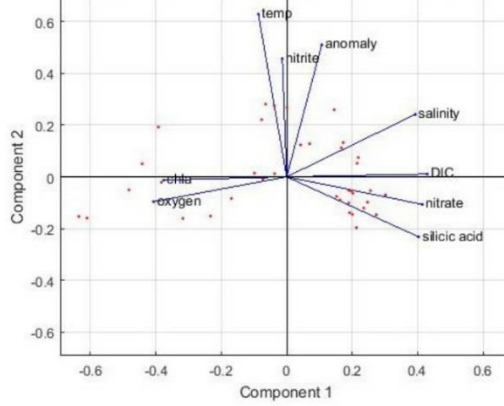
PC1 = 59%

PC2 = 17%

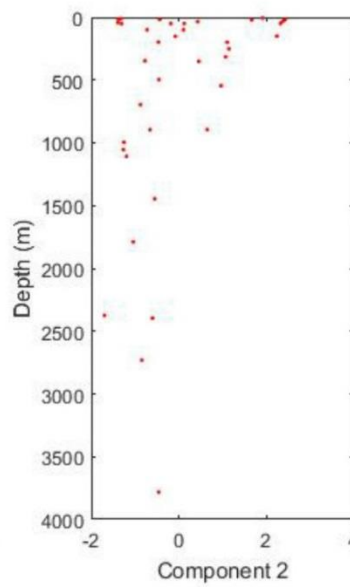
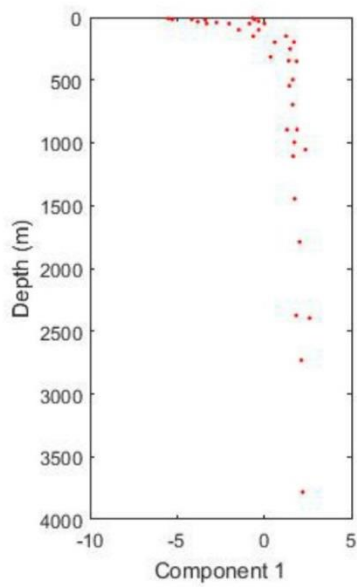
PC3 = 12%

Anomaly PC3 eigenvector <0.1

PCA analysis of meteoric water anomaly and environmental parameters



$$\text{Anomaly} = \%Met_{d^{18}O} - \%Met_{alk}$$



B. Calculation two

Salinities set as per $d^{18}O$ mass balance (see main text)

Meteoric water alkalinity = 159

Seawater alkalinity = 2312

Sea-ice alkalinity = 175

(Alkalinity in $\mu\text{mol}/\text{kg}$;

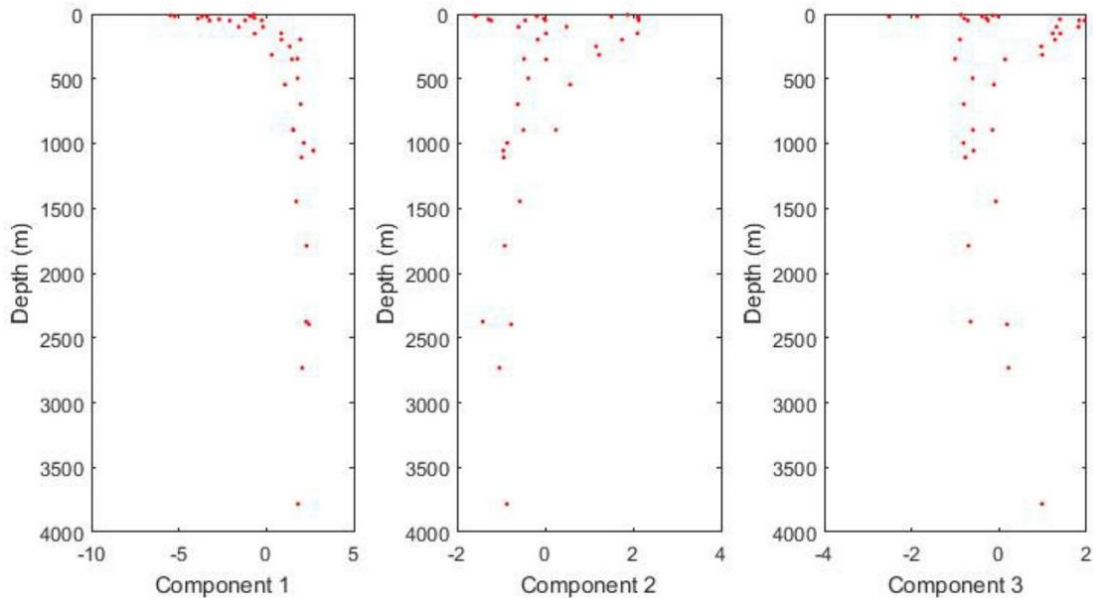
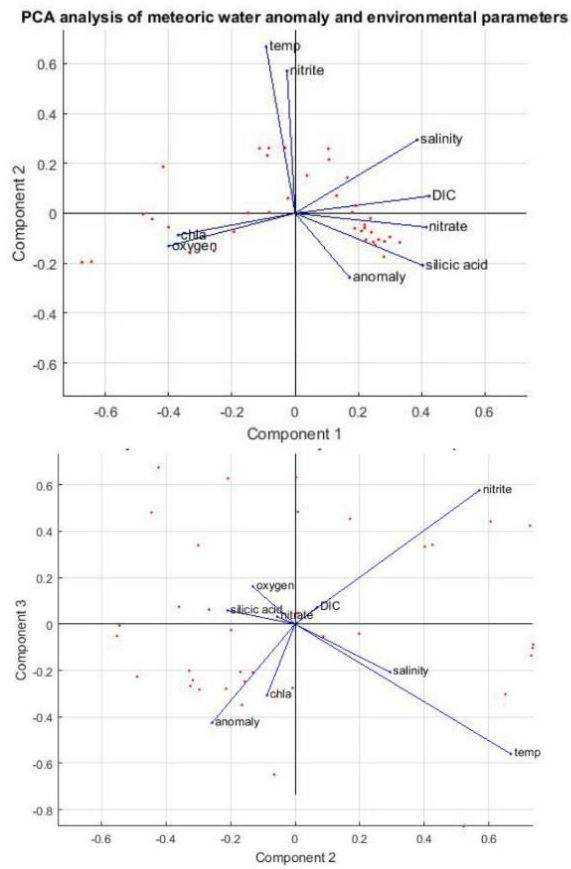
Data from Meire et al., 2015;

Jones et al., 2008)

PC1 = 60%

PC2 = 15%

PC3 = 12%



876

877 Figure A3: Comparison of different freshwater mass balance calculations. Mass balance
 878 calculations were carried out using i) salinity and seawater $\delta^{18}O$ (see main text, Table 1), and
 879 ii) salinity and total alkalinity (TA) measurements:

880
881
882
883
884
885
886
887
888
889
890
891
892
893
894
895
896
897
898
899
900
901
902
903
904

$$F_{ir} + F_{me} + F_{si} = 1$$

$$F_{ir}S_{ir} + F_{me}S_{me} + F_{si}S_{si} = S_{ms}$$

$$F_{ir}A_{ir} + F_{me}A_{me} + F_{si}A_{si} = A_{ms}$$

Where F_{ir} , F_{me} , F_{si} are the calculated fractions of Irminger Water, meteoric and sea ice melt respectively (Irminger Water being the chosen ocean endmember), which sum to 1 by definition. They result is clearly dependent on the exact choice of endmembers for salinity (S_{ir} , S_{me} , S_{si}) and TA (A_{ir} , A_{me} , A_{si}) for the Irminger Water, meteoric and sea ice melt respectively. S_{ms} and A_{ms} are the measured salinity and TA of each sample. Two different calculations were carried out using different end-members for meteoric water alkalinity: A) 1000 $\mu\text{mol/kg}$ (typical value for the Arctic Ocean, from Jones et al., 2008), and B) 159 $\mu\text{mol/kg}$ (glacial meltwater value from Meire et al., 2015). This latter value is more likely to be a robust representation of the end-member in this region compared to the High Arctic as glacial meltwater is likely to dominated meteoric inputs.

The anomaly between the percentage meteoric water was then calculated using:

$$\text{Anomaly} = \%Met_{\delta^{18}\text{O}} - \%Met_{\text{alk}}$$

Principal Component Analysis was then carried out comparing this anomaly with other environmental parameters. Component loadings (lines) and scores (dots) for the main axes are shown (top) together with depth profiles of scores (bottom). Note that the %Met anomalies show strong loading with axes that also show high scores at subsurface depths, and correlate well with nitrite concentrations and temperature. This suggests that the anomalies arise as a result of non-conservative behaviour perhaps associated with water column nitrification or sedimentary denitrification.

905 **Additional references**

906
907

908 Dickson, A.G., Sabine, C.L. and Christian, J.R., 2007. Guide to best practices for ocean CO₂
909 measurements. North Pacific Marine Science Organization.

910 Hendry, K.R., 2017. RRS Discovery Cruise DY081, July 6th – August 8th 2017, National
911 Marine Facilities.

912 Hendry, K.R. et al., 2018. Spatiotemporal Variability of Barium in Arctic Sea-Ice and
913 Seawater. *Journal of Geophysical Research: Oceans*.

914 Henley, S.F. et al., 2018. Macronutrient and carbon supply, uptake and cycling across the
915 Antarctic Peninsula shelf during summer. *Phil. Trans. R. Soc. A*, 376(2122): 20170168.

916 Hydes, D. et al., 2010. Recommendations for the determination of nutrients in seawater to
917 high levels of precision and inter-comparability using continuous flow analysers. GO-
918 SHIP (Unesco/IOC).

919 Krause, J.W., Brzezinski, M.A. and Jones, J.L., 2011. Application of low-level beta counting of
920 ³²Si for the measurement of silica production rates in aquatic environments. *Marine*
921 *Chemistry*, 127(1-4): 40-47.

922 Kuzyk, Z.Z.A., Gobeil, C., Goñi, M.A. and Macdonald, R.W., 2017. Early diagenesis and trace
923 element accumulation in North American Arctic margin sediments. *Geochimica et*
924 *Cosmochimica Acta*, 203: 175-200.

925 Mackereth, F.J.H., Heron, J.t., Talling, J.F. and Association, F.B., 1978. Water analysis: some
926 revised methods for limnologists.

927 McCartney, M., 1992. Recirculating components to the deep boundary current of the
928 northern North Atlantic. *Progress in Oceanography*, 29(4): 283-383.

929 McCartney, M.S. and Talley, L.D., 1982. The subpolar mode water of the North Atlantic
930 Ocean. *Journal of Physical Oceanography*, 12(11): 1169-1188.

931 Meredith, M.P. et al., 2008. Variability in the freshwater balance of northern Marguerite
932 Bay, Antarctic Peninsula: results from d¹⁸O. *Deep-Sea Research II*, 55: 309-322.

933 Sherrell, R.M., Annett, A.L., Fitzsimmons, J.N., Rocanova, V.J. and Meredith, M.P., 2018. A
934 'shallow bathtub ring' of local sedimentary iron input maintains the Palmer Deep
935 biological hotspot on the West Antarctic Peninsula shelf. *Phil. Trans. R. Soc. A*,
936 376(2122): 20170171.

937 Thomas, H. et al., 2011. Barium and carbon fluxes in the Canadian Arctic Archipelago.
938 *Journal of Geophysical Research: Oceans*, 116(C9).

939 Woodward, E. and Rees, A., 2001. Nutrient distributions in an anticyclonic eddy in the
940 northeast Atlantic Ocean, with reference to nanomolar ammonium concentrations.
941 *Deep Sea Research Part II: Topical Studies in Oceanography*, 48(4-5): 775-793.

942 Yang, Q. et al., 2016. Recent increases in Arctic freshwater flux affects Labrador Sea
943 convection and Atlantic overturning circulation. Nature communications, 7:
944 ncomms10525.

945

946

947 **References**

- 948 Alexeev, V.A., Walsh, J.E., Ivanov, V.V., Semenov, V.A., Smirnov, A.V., 2017. Warming in the
949 Nordic Seas, North Atlantic storms and thinning Arctic sea ice. *Environmental Research*
950 *Letters*, 12, 084011.
- 951 Andrews, J., Jennings, A.E., Kerwin, M., Kirby, M., Manley, W., Miller, G., Bond, G., MacLean,
952 B., 1995. A Heinrich-like event, H-0 (DC-0): Source (s) for detrital carbonate in the North
953 Atlantic during the Younger Dryas chronozone. *Paleoceanography*, 10, 943-952.
- 954 Andrews, J.T., Voelker, A.H., 2018. "Heinrich events" (& sediments): A history of terminology
955 and recommendations for future usage. *Quaternary Science Reviews*, 187, 31-40.
- 956 Annett, A.L., Henley, S.F., Van Beek, P., Souhaut, M., Ganeshram, R., Venables, H.J.,
957 Meredith, M.P., Geibert, W., 2013. Use of radium isotopes to estimate mixing rates and
958 trace sediment inputs to surface waters in northern Marguerite Bay, Antarctic Peninsula.
959 *Antarct. Sci*, 25, 445-456.
- 960 Annett, A.L., Skiba, M., Henley, S.F., Venables, H.J., Meredith, M.P., Statham, P.J.,
961 Ganeshram, R.S., 2015. Comparative roles of upwelling and glacial iron sources in Ryder Bay,
962 coastal western Antarctic Peninsula. *Marine Chemistry*, 176, 21-33.
- 963 Arrigo, K.R., van Dijken, G.L., Castelao, R.M., Luo, H., Rennermalm, Å.K., Tedesco, M., Mote,
964 T.L., Oliver, H., Yager, P.L., 2017. Melting glaciers stimulate large summer phytoplankton
965 blooms in southwest Greenland waters. *Geophysical Research Letters*, 44, 6278-6285.
- 966 Bamber, J., Tedstone, A., King, M., Howat, I., Enderlin, E., van den Broeke, M., Noel, B., 2018.
967 Land ice freshwater budget of the Arctic and North Atlantic Oceans: 1. Data, methods, and
968 results. *Journal of Geophysical Research: Oceans*, 123, 1827-1837.
- 969 Berthelsen, T., 2014. Coastal fisheries in Greenland. *KNAPK report, Nuuk*.
- 970 Bhatia, M.P., Kujawinski, E.B., Das, S.B., Breier, C.F., Henderson, P.B., Charette, M.A., 2013.
971 Greenland meltwater as a significant and potentially bioavailable source of iron to the
972 ocean. *Nature Geoscience*, 6, 274.
- 973 Biard, T., Krause, J.W., Stukel, M.R., Ohman, M.D., 2018. The Significance of giant
974 Phaeodarians (Rhizaria) to Biogenic Silica Export in the California Current Ecosystem. *Global*
975 *Biogeochemical Cycles*.
- 976 Biard, T., Stemmann, L., Picheral, M., Mayot, N., Vandromme, P., Hauss, H., Gorsky, G.,
977 Guidi, L., Kiko, R., Not, F., 2016. In situ imaging reveals the biomass of giant protists in the
978 global ocean. *Nature*, 532, 504.
- 979 Bond, G., Broecker, W., Johnsen, S., McManus, J., Labeyrie, L., Jouzel, J., Bonani, G., 1993.
980 Correlations between climate records from North Atlantic sediments and Greenland ice.
981 *Nature*, 365, 143.
- 982 Bond, G., Heinrich, H., Broecker, W.S., Labeyrie, L.D., McManus, J., Andrews, J.E., Huon, S.,
983 Jantschik, R., Clasen, S., Simet, C., Tedesco, K., Klas, M., Bonani, G., Ivy, S., 1992. Evidence for
984 massive discharges of icebergs into the North Atlantic ocean during the last glacial period.
985 *Nature*, 360, 245-249.
- 986 Bond, G.C., Lotti, R., 1995. Iceberg discharges into the North Atlantic on millennial time scales
987 during the last glaciation. *Science*, 267, 1005-1010.
- 988 Broecker, W.S., 2003. Does the trigger for abrupt climate change reside in the ocean or in
989 the atmosphere? *Science*, 300, 1519-1522.
- 990 Broecker, W.S., Bond, G.C., Klas, M., Clark, E., McManus, J., 1992. Origin of the northern
991 Atlantic's Heinrich events. *Climate Dynamics*, 6, 265-273.

992 Brzezinski, M.A., Krause, J.W., Church, M.J., Karl, D.M., Li, B., Jones, J.L., Updyke, B., 2011.
993 The annual silica cycle of the North Pacific subtropical gyre. *Deep Sea Research Part I:*
994 *Oceanographic Research Papers*, 58, 988-1001.

995 Cao, L., Fairbanks, R.G., Mortlock, R.A., Risk, M.J.J.Q.S.R., 2007. Radiocarbon reservoir age of
996 high latitude North Atlantic surface water during the last deglacial. 26, 732-742.

997 Carmack, E.C., Yamamoto-Kawai, M., Haine, T.W., Bacon, S., Bluhm, B.A., Lique, C., Melling,
998 H., Polyakov, I.V., Straneo, F., Timmermans, M.L., 2016. Freshwater and its role in the Arctic
999 Marine System: Sources, disposition, storage, export, and physical and biogeochemical
1000 consequences in the Arctic and global oceans. *Journal of Geophysical Research:*
1001 *Biogeosciences*, 121, 675-717.

1002 Chen, T., Robinson, L.F., Beasley, M.P., Claxton, L.M., Andersen, M.B., Gregoire, L.J.,
1003 Wadham, J., Fornari, D.J., Harpp, K.S.J.S., 2016. Ocean mixing and ice-sheet control of
1004 seawater 234U/238U during the last deglaciation. 354, 626-629.

1005 Clark, P.U., Pisias, N.G., Stocker, T.F., Weaver, A.J., 2002. The role of the thermohaline
1006 circulation in abrupt climate change. *Nature*, 415, 863.

1007 Cuny, J., Rhines, P.B., Kwok, R., 2005. Davis Strait volume, freshwater and heat fluxes. *Deep*
1008 *Sea Research Part I: Oceanographic Research Papers*, 52, 519-542.

1009 Cuny, J., Rhines, P.B., Niiler, P.P., Bacon, S., 2002. Labrador Sea boundary currents and the
1010 fate of the Irminger Sea Water. *Journal of Physical Oceanography*, 32, 627-647.

1011 Dodd, P.A., Heywood, K.J., Meredith, M.P., Naveira-Garabato, A.C., Marca, A.D., Falkner,
1012 K.K., 2009. Sources and fate of freshwater exported in the East Greenland Current.
1013 *Geophysical Research Letters*, 36.

1014 Dowdeswell, J.A., Canals, M., Jakobsson, M., Todd, B., Dowdeswell, E.K., Hogan, K., 2016.
1015 The variety and distribution of submarine glacial landforms and implications for ice-sheet
1016 reconstruction. *Geological Society, London, Memoirs*, 46, 519-552.

1017 Egbert, G.D., Erofeeva, S.Y., 2002. Efficient inverse modeling of barotropic ocean tides.
1018 *Journal of Atmospheric and Oceanic Technology*, 19, 183-204.

1019 Enderlin, E.M., Howat, I.M., Jeong, S., Noh, M.J., Van Angelen, J.H., Van Den Broeke, M.R.,
1020 2014. An improved mass budget for the Greenland ice sheet. *Geophysical Research Letters*,
1021 41, 866-872.

1022 Felikson, D., Bartholomaeus, T.C., Catania, G.A., Korsgaard, N.J., Kjær, K.H., Morlighem, M.,
1023 Noël, B., Van Den Broeke, M., Stearns, L.A., Shroyer, E.L., 2017. Inland thinning on the
1024 Greenland ice sheet controlled by outlet glacier geometry. *Nature Geoscience*, 10, 366.

1025 Fennel, K., Wilkin, J., Previdi, M., Najjar, R., 2008. Denitrification effects on air-sea CO₂ flux
1026 in the coastal ocean: Simulations for the northwest North Atlantic. *Geophysical Research*
1027 *Letters*, 35.

1028 Grousset, F., Labeyrie, L., Sinko, J., Cremer, M., Bond, G., Duprat, J., Cortijo, E., Huon, S.,
1029 1993. Patterns of ice-rafted detritus in the glacial North Atlantic (40–55° N).
1030 *Paleoceanography*, 8, 175-192.

1031 Hawkings, J., Wadham, J., Tranter, M., Telling, J., Bagshaw, E., Beaton, A., Simmons, S.L.,
1032 Chandler, D., Tedstone, A., Nienow, P., 2016. The Greenland Ice Sheet as a hot spot of
1033 phosphorus weathering and export in the Arctic. *Global Biogeochemical Cycles*, 30, 191-210.

1034 Hawkings, J.R., Hatton, J.E., Hendry, K.R., de Souza, G.F., Wadham, J.L., Ivanovic, R., Kohler,
1035 T.J., Stibal, M., Beaton, A., Lamarche-Gagnon, G., 2018. The silicon cycle impacted by past
1036 ice sheets. *Nature Communications*, 9, 3210.

1037 Hawkings, J.R., Wadham, J.L., Benning, L.G., Hendry, K.R., Tranter, M., Tedstone, A., Nienow,
1038 P., Raiswell, R., 2017. Ice sheets as a missing source of silica to the polar oceans. *Nature*
1039 *Communications*, 8, 14198.

1040 Hawkings, J.R., Wadham, J.L., Tranter, M., Raiswell, R., Benning, L.G., Statham, P.J.,
1041 Tedstone, A., Nienow, P., Lee, K., Telling, J., 2014. Ice sheets as a significant source of highly
1042 reactive nanoparticulate iron to the oceans. *Nature Communications*, 5.

1043 Heinrich, H., 1988. Origin and consequences of cyclic ice rafting in the northeast Atlantic
1044 Ocean during the past 130,000 years. *Quaternary Research*, 29, 142-152.

1045 Hendry, K.R., 2017. RRS Discovery Cruise DY081, July 6th – August 8th 2017. National
1046 Marine Facilities.

1047 Hendry, K.R., Pyle, K.M., Barney Butler, G., Cooper, A., Fransson, A., Chierici, M., Leng, M.J.,
1048 Meyer, A., Dodd, P.A., 2018. Spatiotemporal Variability of Barium in Arctic Sea-Ice and
1049 Seawater. *Journal of Geophysical Research: Oceans*.

1050 Henley, S.F., Jones, E.M., Venables, H.J., Meredith, M.P., Firing, Y.L., Dittrich, R., Heiser, S.,
1051 Stefels, J., Dougans, J., 2018. Macronutrient and carbon supply, uptake and cycling across
1052 the Antarctic Peninsula shelf during summer. *Phil. Trans. R. Soc. A*, 376, 20170168.

1053 Hillaire-Marcel, C., Bilodeau, G., 2000. Instabilities in the Labrador Sea water mass structure
1054 during the last climatic cycle. *Canadian Journal of Earth Sciences*, 37, 795-809.

1055 Hillaire-Marcel, C., Maccali, J., Ménabréaz, L., Ghaleb, B., Blénet, A., Edinger, E., 2017. U-
1056 series vs ¹⁴C ages of deep-sea corals from the southern Labrador Sea: Sporadic
1057 development of corals and geochemical processes hampering estimation of ambient water
1058 ventilation ages. *EGU General Assembly Conference Abstracts*, Vol. 19 (p. 9126).

1059 Hodell, D.A., Channell, J.E., Curtis, J.H., Romero, O.E., Röhl, U., 2008. Onset of “Hudson
1060 Strait” Heinrich events in the eastern North Atlantic at the end of the middle Pleistocene
1061 transition (~ 640 ka)? *Paleoceanography*, 23.

1062 Hopwood, M.J., Bacon, S., Arendt, K., Connelly, D., Statham, P., 2015. Glacial meltwater
1063 from Greenland is not likely to be an important source of Fe to the North Atlantic.
1064 *Biogeochemistry*, 124, 1-11.

1065 Hopwood, M.J., Carroll, D., Browning, T.J., Meire, L., Mortensen, J., Krisch, S., Achterberg,
1066 E.P., 2018. Non-linear response of summertime marine productivity to increased meltwater
1067 discharge around Greenland. *Nature Communications*, 9, 3256.

1068 Jones, E., Anderson, L., Jutterström, S., Swift, J., 2008. Sources and distribution of fresh
1069 water in the East Greenland Current. *Progress in Oceanography*, 78, 37-44.

1070 Katsman, C.A., Spall, M.A., Pickart, R.S., 2004. Boundary current eddies and their role in the
1071 restratification of the Labrador Sea. *Journal of Physical Oceanography*, 34, 1967-1983.

1072 Kenchington, E., Yashayaev, I., Tendal, O.S., Jørgensbye, H., 2017. Water mass
1073 characteristics and associated fauna of a recently discovered *Lophelia pertusa* (Scleractinia:
1074 Anthozoa) reef in Greenlandic waters. *Polar Biology*, 40, 321-337.

1075 Krause, J.W., Brzezinski, M.A., Jones, J.L., 2011. Application of low-level beta counting of
1076 ³²Si for the measurement of silica production rates in aquatic environments. *Marine*
1077 *Chemistry*, 127, 40-47.

1078 Krause, J.W., Duarte, C.M., Marquez, I.A., Assmy, P., Fernández-Méndez, M., Wiedmann, I.,
1079 Wassmann, P., Kristiansen, S., Agustí, S., 2018. Biogenic silica production and diatom
1080 dynamics in the Svalbard region during spring. *Biogeosciences*, 15, 6503-6517.

1081 Krause, J.W., Nelson, D.M., Lomas, M.W., 2010. Production, dissolution, accumulation, and
1082 potential export of biogenic silica in a Sargass Sea mode-water eddy. *Limnology and*
1083 *Oceanography*, 55, 569-579.

1084 Krause, J.W., Schulz, I.K., Rowe, K.A., Dobbins, W., Winding, M., Sejr, M., Duarte, C.M.,
1085 Agustí, S., In review. Silicon limitation drives bloom termination and carbon sequestration in
1086 an Arctic bloom. *Scientific reports*.

1087 Kuzyk, Z.Z.A., Gobeil, C., Goñi, M.A., Macdonald, R.W., 2017. Early diagenesis and trace
1088 element accumulation in North American Arctic margin sediments. *Geochimica et*
1089 *Cosmochimica Acta*, 203, 175-200.

1090 Lindsay, R., Schweiger, A., 2015. Arctic sea ice thickness loss determined using subsurface,
1091 aircraft, and satellite observations. *The Cryosphere*, 9, 269-283.

1092 Luo, H., Castelao, R.M., Rennermalm, A.K., Tedesco, M., Bracco, A., Yager, P.L., Mote, T.L.,
1093 2016. Oceanic transport of surface meltwater from the southern Greenland ice sheet.
1094 *Nature Geoscience*, 9, 528.

1095 Lynch-Stieglitz, J., Schmidt, M.W., Henry, L.G., Curry, W.B., Skinner, L.C., Mulitza, S., Zhang,
1096 R., Chang, P., 2014. Muted change in Atlantic overturning circulation over some glacial-aged
1097 Heinrich events. *Nature Geoscience*, 7, 144.

1098 Maslanik, J., Fowler, C., Stroeve, J., Drobot, S., Zwally, J., Yi, D., Emery, W., 2007. A younger,
1099 thinner Arctic ice cover: Increased potential for rapid, extensive sea-ice loss. *Geophysical*
1100 *Research Letters*, 34.

1101 McManus, J.F., Anderson, R.F., Broecker, W.S., Fleisher, M.Q., Higgins, S.M., 1998.
1102 Radiometrically determined sedimentary fluxes in the sub-polar North Atlantic during the
1103 last 140,000 years. *Earth and Planetary Science Letters*, 155, 29-43.

1104 McManus, J.F., Francois, R., Gherardi, J.-M., Keigwin, L.D., Brown-Leger, S., 2004. Collapse
1105 and rapid resumption of Atlantic meridional circulation linked to deglacial climate changes.
1106 *Nature*, 428, 834-837.

1107 Meire, L., Meire, P., Struyf, E., Krawczyk, D., Arendt, K., Yde, J., Juul Pedersen, T., Hopwood,
1108 M.J., Rysgaard, S., Meysman, F., 2016. High export of dissolved silica from the Greenland Ice
1109 Sheet. *Geophysical Research Letters*, 43, 9173-9182.

1110 Meire, L., Mortensen, J., Meire, P., Juul-Pedersen, T., Sejr, M.K., Rysgaard, S., Nygaard, R.,
1111 Huybrechts, P., Meysman, F.J., 2017. Marine-terminating glaciers sustain high productivity
1112 in Greenland fjords. *Global Change Biology*, 23, 5344-5357.

1113 Meire, L., Søgaard, D., Mortensen, J., Meysman, F., Soetaert, K., Arendt, K., Juul-Pedersen,
1114 T., Blicher, M., Rysgaard, S., 2015. Glacial meltwater and primary production are drivers of
1115 strong CO₂ uptake in fjord and coastal waters adjacent to the Greenland Ice Sheet.
1116 *Biogeosciences*, 12, 2347-2363.

1117 Melling, H., Moore, R.M., 1995. Modification of halocline source waters during freezing on
1118 the Beaufort Sea shelf: evidence from oxygen isotopes and dissolved nutrients. *Continental*
1119 *Shelf Research*, 15, 89-113.

1120 Meredith, M., Heywood, K., Dennis, P., Goldson, L., White, R., Fahrbach, E., Schauer, U.,
1121 Østerhus, S., 2001. Freshwater fluxes through the western Fram Strait. *Geophysical*
1122 *Research Letters*, 28, 1615-1618.

1123 Meredith, M.P., Brandon, M.A., Wallace, M.I., Clarke, A., Leng, M.J., Renfrew, I.A., van Lipzig,
1124 N.P.M., King, J.C., 2008. Variability in the freshwater balance of northern Marguerite Bay,
1125 Antarctic Peninsula: results from d¹⁸O. *DEep-Sea Research II*, 55, 309-322.

1126 Moore, W.S., 2008. Fifteen years experience in measuring ²²⁴Ra and ²²³Ra by delayed-
1127 coincidence counting. *Marine Chemistry*, 109, 188-197.

1128 Moore, W.S., Arnold, R., 1996. Measurement of ²²³Ra and ²²⁴Ra in coastal waters using a
1129 delayed coincidence counter. *Journal of Geophysical Research: Oceans*, 101, 1321-1329.

1130 Moros, M., Kuijpers, A., Snowball, I., Lassen, S., Bäckström, D., Gingele, F., McManus,
1131 J.J.M.G., 2002. Were glacial iceberg surges in the North Atlantic triggered by climatic
1132 warming? , 192, 393-417.

1133 Moros, M., McManus, J., Rasmussen, T., Kuijpers, A., Dokken, T., Snowball, I., Nielsen, T.,
1134 Jansen, E., 2004. Quartz content and the quartz-to-plagioclase ratio determined by X-ray
1135 diffraction: a proxy for ice rafting in the northern North Atlantic? *Earth and Planetary
1136 Science Letters*, 218, 389-401.

1137 Myers, P.G., Donnelly, C., Ribergaard, M.H., 2009. Structure and variability of the West
1138 Greenland Current in Summer derived from 6 repeat standard sections. *Progress in
1139 Oceanography*, 80, 93-112.

1140 Nelson, D.M., Treguer, P., Brzezinski, M.A., Leynaert, A., Queguiner, B., 1995. Production
1141 and dissolution of biogenic silica in the ocean: revised global estimates, comparison with
1142 regional data and relationship to biogenic sedimentation. *Global Biogeochemical Cycles*, 9,
1143 359-372.

1144 Oliver, H., Luo, H., Castelao, R.M., van Dijken, G.L., Mattingly, K.S., Rosen, J.J., Mote, T.L.,
1145 Arrigo, K.R., Rennermalm, Å.K., Tedesco, M., 2018. Exploring the Potential Impact of
1146 Greenland Meltwater on Stratification, Photosynthetically Active Radiation, and Primary
1147 Production in the Labrador Sea. *Journal of Geophysical Research: Oceans*, 123, 2570-2591.

1148 Proshutinsky, A., Dukhovskoy, D., Timmermans, M.-L., Krishfield, R., Bamber, J.L., 2015.
1149 Arctic circulation regimes. *Phil. Trans. R. Soc. A*, 373, 20140160.

1150 Provost, C., Sennéchaël, N., Miguët, J., Itkin, P., Rösel, A., Koenig, Z., Villacieros-Robineau,
1151 N., Granskog, M.A., 2017. Observations of flooding and snow-ice formation in a thinner
1152 Arctic sea ice regime during the N-ICE2015 campaign: Influence of basal ice melt and storms.
1153 *Journal of Geophysical Research: Oceans*.

1154 Ragueneau, O., Gallinari, M., Corrin, L., Grandel, S., Hall, P., Hauvespre, A., Lampitt, R.,
1155 Rickert, D., Stahl, H., Tengberg, A., 2001. The benthic silica cycle in the Northeast Atlantic:
1156 annual mass balance, seasonality, and importance of non-steady-state processes for the
1157 early diagenesis of biogenic opal in deep-sea sediments. *Progress in Oceanography*, 50, 171-
1158 200.

1159 Rahman, S., Aller, R., Cochran, J., 2017. The missing silica sink: revisiting the marine
1160 sedimentary Si cycle using cosmogenic ³²Si. *Global Biogeochemical Cycles*.

1161 Rashid, H., Hesse, R., Piper, D.J., 2003. Evidence for an additional Heinrich event between H5
1162 and H6 in the Labrador Sea. *Paleoceanography*, 18.

1163 Robinson, L.F., Adkins, J.F., Frank, N., Gagnon, A.C., Prouty, N.G., Roark, E.B., van de Flierdt,
1164 T.J.D.S.R.P.I.T.S.i.O., 2014. The geochemistry of deep-sea coral skeletons: a review of vital
1165 effects and applications for palaeoceanography. 99, 184-198.

1166 Ruddiman, W.F., Sancetta, C., McIntyre, A., 1977. Glacial/interglacial response rate of
1167 subpolar North Atlantic waters to climatic change: the record in oceanic sediments. *Phil.
1168 Trans. R. Soc. Lond. B*, 280, 119-142.

1169 Ryan, J., Dowdeswell, J., Hogan, K., 2016. Three cross-shelf troughs on the continental shelf
1170 of SW Greenland from Olex data. *Geological Society, London, Memoirs*, 46, 167-168.

1171 Rykova, T., Straneo, F., Bower, A.S., 2015. Seasonal and interannual variability of the West
1172 Greenland Current System in the Labrador Sea in 1993–2008. *Journal of Geophysical
1173 Research: Oceans*, 120, 1318-1332.

1174 Schofield, O., Ducklow, H., Bernard, K., Doney, S., Patterson-Fraser, D., Gorman, K.,
1175 Martinson, D., Meredith, M., Saba, G., Stammerjohn, S., 2013. Penguin biogeography along

1176 the West Antarctic Peninsula: Testing the canyon hypothesis with Palmer LTER observations.
1177 *Oceanography*, 26, 204-206.

1178 Schulze, L.M., Frajka-Williams, E., 2018. Wind-driven transport of fresh shelf water into the
1179 upper 30m of the Labrador Sea. *Ocean Science*, 14(5), 1247-1264.

1180 Sherrell, R.M., Annett, A.L., Fitzsimmons, J.N., Roccanova, V.J., Meredith, M.P., 2018. A
1181 'shallow bathtub ring' of local sedimentary iron input maintains the Palmer Deep biological
1182 hotspot on the West Antarctic Peninsula shelf. *Phil. Trans. R. Soc. A*, 376, 20170171.

1183 Stoner, J.S., Channell, J.E., Hillaire-Marcel, C., 1996. The magnetic signature of rapidly
1184 deposited detrital layers from the deep Labrador Sea: Relationship to North Atlantic
1185 Heinrich layers. *Paleoceanography and Paleoclimatology*, 11, 309-325.

1186 Thomas, H., Shadwick, E., Dehairs, F., Lansard, B., Mucci, A., Navez, J., Gratton, Y., Prowe, F.,
1187 Chierici, M., Fransson, A., 2011. Barium and carbon fluxes in the Canadian Arctic
1188 Archipelago. *Journal of Geophysical Research: Oceans*, 116.

1189 Van As, D., Andersen, M.L., Petersen, D., Fettweis, X., Van Angelen, J.H., Lenaerts, J.T., Van
1190 Den Broeke, M.R., Lea, J.M., Bøggild, C.E., Ahlstrøm, A.P., 2014. Increasing meltwater
1191 discharge from the Nuuk region of the Greenland ice sheet and implications for mass
1192 balance (1960–2012). *Journal of Glaciology*, 60, 314-322.

1193 van den Broeke, M., Box, J., Fettweis, X., Hanna, E., Noël, B., Tedesco, M., van As, D., van de
1194 Berg, W.J., van Kampenhout, L., 2017. Greenland ice sheet surface mass loss: recent
1195 developments in observation and modeling. *Current Climate Change Reports*, 3, 345-356.

1196 Wadham, J.L., Hawkings, J., Telling, J., Chandler, D., Alcock, J., Lawson, E., Kaur, P., Bagshaw,
1197 E., Tranter, M., Tedstone, A., 2016. Sources, cycling and export of nitrogen on the Greenland
1198 Ice Sheet. *Biogeosciences Discussions*.

1199 Wang, Y.-J., Cheng, H., Edwards, R.L., An, Z., Wu, J., Shen, C.-C., Dorale, J.A., 2001. A high-
1200 resolution absolute-dated late Pleistocene monsoon record from Hulu Cave, China. *Science*,
1201 294, 2345-2348.

1202 Weatherdon, L.V., Magnan, A.K., Rogers, A.D., Sumaila, U.R., Cheung, W.W., 2016. Observed
1203 and projected impacts of climate change on marine fisheries, aquaculture, coastal tourism,
1204 and human health: an update. *Frontiers in Marine Science*, 3, 48.

1205 Wolf-Gladrow, D.A., Zeebe, R.E., Klaas, C., Körtzinger, A., Dickson, A.G.J.M.C., 2007. Total
1206 alkalinity: The explicit conservative expression and its application to biogeochemical
1207 processes. 106, 287-300.

1208 Yang, Q., Dixon, T.H., Myers, P.G., Bonin, J., Chambers, D., Van Den Broeke, M., Ribergaard,
1209 M.H., Mortensen, J., 2016. Recent increases in Arctic freshwater flux affects Labrador Sea
1210 convection and Atlantic overturning circulation. *Nature Communications*, 7, ncomms10525.

1211